

Review

Influence of Chemical Substitution and Light Element Insertion on the Magnetic Properties of Nanocrystalline Pr₂Co₇ Compound

Riadh Fersi ^{1,2}, Najeh Mliki ²  and Lotfi Bessais ^{1,*} 

¹ Department of Physics, University Paris Est Creteil, CNRS, ICMPE, 2 Rue Henri Dunant, F-94320 Thiais, France; riadh.fersi@fst.utm.tn

² Laboratory of Materials Organization and Properties, Faculty of Science of Tunis, University of Tunis El Manar, Tunis 2092, Tunisia; najeh.mliki@fst.utm.tn

* Correspondence: bessais@icmpe.cnrs.fr; Tel.: +33-1-4978-1197

Abstract: It is well recognized that intermetallics based on rare-earth (R) and transition metals (T) display numerous interesting magnetic properties, leading to potential applications in different fields. The latest progress regarding magnetic properties and the magnetocaloric effect (MCE) in the nanostructured Pr₂Co₇ compound, as well as its carbides and hydrides, is reviewed in this paper. Some of this progress reveals remarkable MCE performance, which makes it attractive in the field of magnetic refrigeration at high temperatures. With the purpose of understanding the magnetic and magnetocaloric characteristics of these compounds, the crystal structure, microstructure, and magnetism are also brought into focus. The Pr₂Co₇ compound has interesting magnetic properties, such as a high Curie temperature T_C and uniaxial magnetocrystalline anisotropy. It crystallizes in a hexagonal structure (2:7 H) of the Ce₂Ni₇ type and is stable at relatively low temperatures (T_a ≤ 1023 K), or it has a rhombohedral structure (2:7 R) of the Gd₂Co₇ type and is stable at high temperatures (T_a ≥ 1223 K). Studies of the magnetocaloric properties of the nanocrystalline Pr₂Co₇ compound have shown the existence of a large reversible magnetic entropy change (ΔS_M) with a second-order magnetic transition. After its substitution, we showed that nanocrystalline Pr₂Co_{7-x}Fe_x compounds that were annealed at T_a = 973 K crystallized in the 2:7 H structure similarly to the parent compound. The extended X-ray absorption fine-structure (EXAFS) spectra adjustments showed that Fe atoms preferably occupy the 12k site for x ≤ 1. The study of the magnetic properties of nanocrystalline Pr₂Co_{7-x}Fe_x compounds revealed an increase in T_C of about 26% for x = 0.5, as well as an improvement in the coercivity, H_c (12 kOe), and the (BH)_{max} (9 MGOe) product. On the other hand, the insertion of C atoms into the Pr₂Co₇ cell led to a marked improvement in the T_C value of 21.6%. The best magnetic properties were found for the Pr₂Co₇C_{0.25} compound annealed at 973 K, H_c = 10.3 kOe, and (BH)_{max} = 11.5 MGOe. We studied the microstructure, hydrogenation, and magnetic properties of nanocrystalline Pr₂Co₇H_x hydrides. The crystal structure of the Pr₂Co₇ compound transformed from a hexagonal (P6₃/mmc) into an orthorhombic (Pbcn) and monoclinic (C2/c) structure during hydrogenation. The absorption of H by the Pr₂Co₇ compound led to an increase in the T_C value from 600 K at x = 0 to 691 K at x = 3.75. The Pr₂Co₇H_{0.25} hydride had optimal magnetic properties: H_c = 6.1 kOe, (BH)_{max} = 5.8 MGOe, and T_C = 607 K. We tailored the mean field theory (MFT) and random magnetic anisotropy (RMA) methods to investigate the magnetic moments, exchange interactions, and magnetic anisotropy properties. The relationship between the microstructure and magnetic properties is discussed. The obtained results provide a fundamental reference for adapting the magnetic properties of the Pr₂Co₇, Pr₂Co_{6.5}Fe_{0.5}, Pr₂Co₇C_{0.25}, and Pr₂Co₇H_{0.25} compounds for potential permanent nanomagnets, high-density magnetic recording, and magnetic refrigeration applications.

Keywords: intermetallics; nanomaterials; microstructural properties; magnetic properties; magnetocaloric properties



Citation: Fersi, R.; Mliki, N.; Bessais, L. Influence of Chemical Substitution and Light Element Insertion on the Magnetic Properties of Nanocrystalline Pr₂Co₇ Compound. *Magnetochemistry* **2022**, *8*, 20. <https://doi.org/10.3390/magnetochemistry8020020>

Academic Editor: Adriana Greco

Received: 21 December 2021

Accepted: 20 January 2022

Published: 27 January 2022

Publisher's Note: MDPI stays neutral with regard to jurisdictional claims in published maps and institutional affiliations.



Copyright: © 2022 by the authors. Licensee MDPI, Basel, Switzerland. This article is an open access article distributed under the terms and conditions of the Creative Commons Attribution (CC BY) license (<https://creativecommons.org/licenses/by/4.0/>).

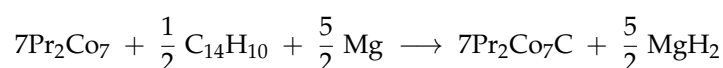
1. Introduction

In recent years, magnetic nanomaterials based on rare-earth elements (R) and transition metals (T) have been widely investigated due to their extremely diverse potential applications in industrial fields [1–8]. These properties are often used to produce soft, hard, or semi-hard magnetic materials [9–23]. The origin of these exceptional magnetic properties is particularly due to the coexistence of two complementary kinds of magnetism: the localized magnetism characteristic of rare-earth (R) electrons and the itinerant magnetism of the 3d electrons of transition metals (T), such as cobalt (Co) and iron (Fe) [24–33]. The R elements thus provide their strong magnetocrystalline anisotropy (H_a) due to the interactions between their orbital moment and the crystal field. The 3d metals provide their strong magnetization and a high Curie temperature (T_C) due to the important exchange interactions between the 3d elements [34–51]. Permanent magnets are the idea of an ever-increasing number of recent devices. Alloys and intermetallic compounds obtained by combining (R) elements with metals (T) form a crucial class of materials for which applications have been found in permanent magnets [44]. Among the intermetallic systems, the noncrystalline Pr_2Co_7 compound is currently one of the most promising [34,52–54]. The interest in these systems is due to the combination of the complementary characteristics of the 3d-itinerant and 4f-localized magnetism of Co and Pr atoms, respectively [54,55]. In order to strengthen these interactions, it is necessary to partially substitute the Co atoms in the noncrystalline Pr_2Co_7 compounds with an appropriate element, such as iron (Fe), or through the insertion of a light element, such as carbon (C) or hydrogen (H), which can increase interatomic distances and strengthen the magnetic moment.

In addition, in parallel with the optimization of the intrinsic magnetic properties, it is necessary to optimize the extrinsic magnetic properties of the Pr_2Co_7 , $\text{Pr}_2\text{Co}_{7-x}\text{Fe}_x$, $\text{Pr}_2\text{Co}_7\text{C}_x$, and $\text{Pr}_2\text{Co}_7\text{H}_x$ compounds by searching for a suitable nanocrystalline state corresponding to the potential applications. In our study, we implemented the high-energy grinding technique followed by controlled recrystallization. At this scale, the grain size was brought to the order of magnitude of the exchange length. This method, which constitutes a non-equilibrium synthesis process, makes it possible to obtain metastable nanostructured powders from a mixture of elementary powders. We tailored the mean field theory (MFT) [56,57] and random magnetic anisotropy (RMA) [58,59] to investigate the magnetic moments, exchange interactions, and magnetic anisotropy properties. The correlation between microstructure and magnetic properties is discussed. The magnetocaloric properties for the nanocrystalline Pr_2Co_7 compound are reported. The magnetocaloric effect is calculated in terms of isothermal magnetic entropy change (ΔS_M^{max}) based on the magnetization isotherms obtained at different temperatures for the rhombohedral (2:7 R) and hexagonal structures (2:7 H). Furthermore, we discuss the impact of stacking blocks on low-field magnetic refrigeration in the nanocrystalline Pr_2Co_7 compound.

2. Synthesis Methods of Pr_2Co_7 , $\text{Pr}_2\text{Co}_{7-x}\text{Fe}_x$, $\text{Pr}_2\text{Co}_x\text{C}_x$, and $\text{Pr}_2\text{Co}_x\text{H}_x$ Samples

To prepare the nanocrystalline Pr_2Co_7 and $\text{Pr}_2\text{Co}_{7-x}\text{Fe}_x$ ($x = 0.25, 0.5, 0.75$, and 1) samples, high-energy ball milling was carried out on previously prepared ingots [60]. The pre-alloy obtained by fusion was broken inside a glove box with a mortar and then introduced with five beads into a hermetically sealed jar. A Fritsch P7 planetary mill with a bead/powder ratio of 15:1 was used to get finer particles. The ground powder was then wrapped in tantalum foil (Ta) and then sealed in quartz ampoules under secondary vacuum (10^{-6} bar) at different annealing temperatures: $T_a = 700$ K and 1350 K. The tantalum foil (Ta) was used to avoid contamination due to contact with silica; these samples were first degassed under secondary vacuum to ensure that no impurities came to pollute the synthesis products. The sample was cooled after leaving the oven by quenching in water. To insert carbon atoms (C) into the Pr_2Co_7 elemental cell, we used a carbonation technique that involved a solid–solid-type reaction according to the following reaction [61]:



Hydrogen atoms (H) were inserted into the Pr_2Co_7 compound with a solid–gas reaction between the sample and 99.99% pure dihydrogen (H_2) [58]. The method used was that of Sievert [62,63]. The amount of absorbed hydrogen was determined with a volumetric method [64,65].

3. Structural, Microstructural, and Magnetic Characterizations of the Samples

The microstructural characterizations of the Pr_2Co_7 , $\text{Pr}_2\text{Co}_{7-x}\text{Fe}_x$, $\text{Pr}_2\text{Co}_x\text{C}_x$, and $\text{Pr}_2\text{Co}_x\text{H}_x$ samples were investigated by using X-ray diffraction (XRD; Bruker D8 Advance) with CuK_α radiation of wavelength $\lambda = 0.154056$ nm. The refinement of the patterns was done by using the FULLPROF computing code based on the Rietveld method [66,67] with the assumption of the Thompson–Cox–Hastings line profile. The goodness-of-fit indicators χ^2 and R_B were calculated as previously described in [61]. Extended X-ray absorption fine-structure (EXAFS) measurements were performed on a 2.75 GeV SAMBA beamline, Synchrotron SOLEIL, France. EXAFS experiments were carried out at 293 K in the fluorescence mode using a 4-element Si(111) drift detector. The EXAFS spectra were extrapolated using the MAXeCherokee code [68,69], while the fitting process and comparison between theoretical and experimental EXAFS curves were carried out with the MAX-Roundmidnight package [68]. The theoretical phases and amplitudes used in the EXAFS models were determined with the FEFF8 code [70] by using the crystal structure results of the Rietveld refinements at each Fe site with the use of the MAX-CRYSTALFFREX code [68] for the Crystal Structure–EXAFS Modeling interface.

The morphology, the chemical compositions, and the images were considered using a JEOL 2010 FEG transmission electron microscope equipped with an energy-dispersive spectrometer (EDS). For the TEM measurements, specimens were thinned using a focused-ion-beam-type FEI Helios 600 Nanolab dual-beam instrument. The Curie temperature T_C was measured on a MANICS differential sample magnetometer (DSM-871 Magneto/susceptometer) in a field of 1 kOe with a sample of around $5\text{--}10 \times 10^{-3}$ g. T_C was obtained from the $M(T)$ curve by extracting the linear part of the $M(T)$ curve and determining the temperature value of the intersection with the expanded baseline. Magnetic hysteresis $M(H)$ loops were determined using a Physical Properties Measurement System (PPMS9) Quantum Design microscope.

4. Structural Properties

4.1. Nanocrystalline Pr_2Co_7 Compound

The nanocrystalline Pr_2Co_7 compound can crystallize into two polymorphic structures [54] as a function of the annealing temperature T_a ; the first is a hexagonal (2:7 H) structure of the Ce_2Ni_7 type ($P6_3/mmc$ space group) that is stable at $T_a \leq 1023$ K with the lattice parameters $a = b = 5.068$ Å and $c = 24.463$ Å. The second is a rhombohedral (2:7 R) structure of the Gd_2Co_7 type ($R\bar{3}m$ space group) that is stable at $T_a \geq 1223$ K. The lattice parameters are $a = b = 5.068$ Å and $c = 36.549$ Å. The Pr_2Co_7 cells can be defined by stacking the hexagonal structural blocks for PrCo_5 (CaCu_5 -type structure) and the cubic PrCo_2 blocks (MgCu_2 - and MgZn_2 -type structures) along the common hexagonal (trigonal for PrCo_2) axis [54]. The lattice parameters of the two structures are distinguished by the c parameter, which is higher for the 2:7 R structure due to the difference in stacking ($[2\text{H}] = [\text{BBA}_1\text{BBA}_2]$, $[3\text{R}_i] = 3[\text{BBA}_1]$) [71–73].

4.2. Nanocrystalline $\text{Pr}_2\text{Co}_{7-x}\text{Fe}_x$ ($x = 0, 0.25, 0.5, 0.75$, and 1) Compounds

The analysis performed with XRD for the nanocrystalline $\text{Pr}_2\text{Co}_{7-x}\text{Fe}_x$ ($x = 0, 0.25, 0.5, 0.75$, and 1) compounds annealed at $T_a = 973$ K showed the presence of a main crystallographic phase with the structure of Ce_2Ni_7 ($P6_3/mmc$ space group) [69,71]. The peaks found were identified by assigning Miller indices (hkl) to the different peaks recorded. Using Rietveld analysis, we were able to determine the crystallographic parameters for each compound. The structural results and the R_B and χ_2 parameters are listed in Table 1. The minimum of the R_B and χ_2 parameters corresponded to Fe located in the $6h$ position,

which indicated that $6h$ was the preferential site for Fe. The $\text{Pr}_2\text{Co}_{7-x}\text{Fe}_x$ unit cell expansion was about 1.15%. The variation of the c/a ratio with x suggested that the unit cell expansion was anisotropic and more pronounced in the basal plane. The grain size Φ was estimated from Scherrer's expression [61,63]: $\Phi = 0.9 \lambda / (\beta_L \cdot \cos\theta)$, where β_L is the full width at half maximum (FWHM) of the peaks at the diffraction angle θ . The Φ values were around 125, 130, 140, 146, and 154 nm for $x = 0, 0.25, 0.50, 0.75,$ and 1 , respectively. For $1 < x < 2.5$, the multiphase sample formation was highlighted by additional diffraction peaks that were not indexed in the $P6_3/mmc$ space group. We noted the appearance of additional lines corresponding to the reflections of the 1:3 structure. For $x > 2.5$, we noted the appearance of other peaks that were similar to those corresponding to the 1:3 and 2:17 phases. The 2:7 structure disappeared entirely and broke down into $\text{Pr}(\text{Co,Fe})_3 + \text{Pr}_2(\text{Co,Fe})_{17}$ [69].

Table 1. Structural data from the Rietveld analysis of nanocrystalline $\text{Pr}_2\text{Co}_{7-x}\text{Fe}_x$ compounds.

| x | 0.0 | 0.25 | 0.5 | 0.75 | 1 |
|-----------------------|-----------|-----------|-----------|-----------|-----------|
| a (Å) | 5.068(3) | 5.068(2) | 5.076(3) | 5.078(1) | 5.102(2) |
| c (Å) | 24.458(2) | 24.462(4) | 24.473(5) | 24.474(3) | 24.475(4) |
| c/a | 4.826 | 4.827 | 4.822 | 4.826 | 4.785 |
| V (Å ³) | 544.02 | 544.08 | 546.09 | 546.56 | 550.18 |
| R_B | 3.2 | 2.7 | 1.7 | 2.865 | 2.437 |
| χ^2 | 3.80 | 3.72 | 3.58 | 3.52 | 3.68 |

Figure 1 presents bright-field micrographs of the $\text{Pr}_2\text{Co}_{7-x}\text{Fe}_{0.75}$ (Figure 1a) compound. By performing statistical calculations on the grain size, the grain size distributions are shown in Figure 1b. The grain size Φ_{TEM} was estimated to be 90 nm. The values found are in good agreement with the average grain sizes found using Scherrer's expression. The HRTEM images shown in Figure 2a,b reveal the fully crystallized structure of the $\text{Pr}_2\text{Co}_{6.25}\text{Fe}_{0.75}$ and $\text{Pr}_2\text{Co}_6\text{Fe}_1$ compounds. The composition distribution was investigated by STEM-EDX mapping (Figure 2c–e). The stoichiometric proportions of $\text{Pr}_2\text{Co}_{7-x}\text{Fe}_x$ were maintained. The Pr, Co, and Fe compositions ranged from 20.8 to 23.5%, 78.9 to 75.5%, and 1.4 to 2.6%, respectively. The diffraction spots were distributed over the rings corresponding to the d_{107} (0.795 nm), d_{110} (0.635 nm), d_{201} (0.508 nm), d_{116} (0.458 nm), d_{0012} (0.291 nm), d_{1110} (0.258 nm), and d_{217} (0.158 nm) distances for the (2:7 H) structure [69].

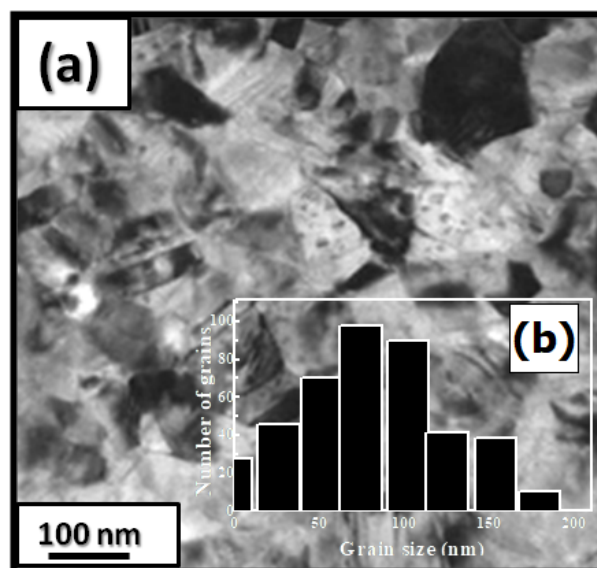


Figure 1. Bright-field micrograph of the $\text{Pr}_2\text{Co}_{6.25}\text{Fe}_{0.75}$ compound (a). The grain size distribution is shown in the inset (b).

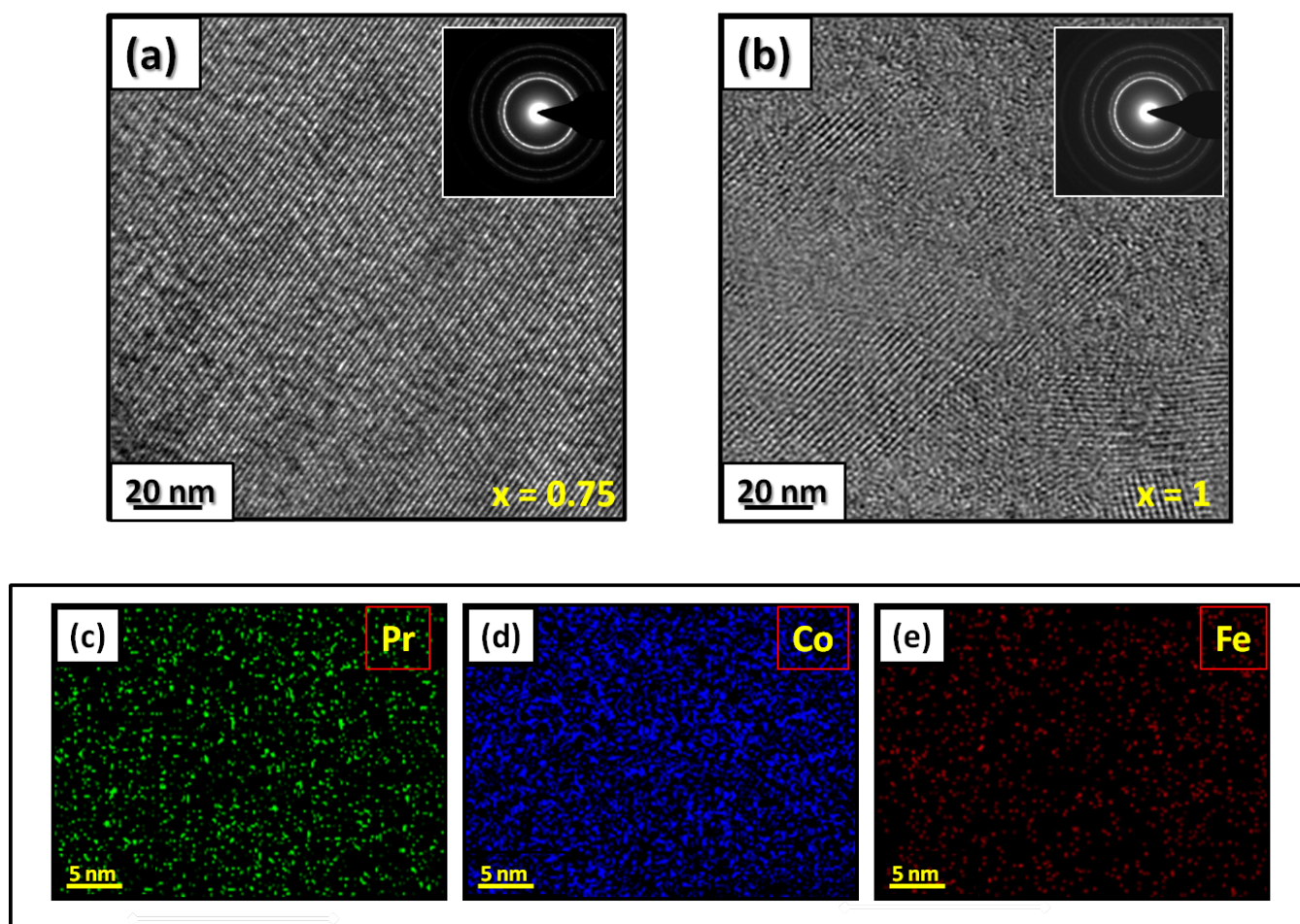


Figure 2. HRTEM images (the selected area of electron diffraction is shown in the inset): (a) $\text{Pr}_2\text{Co}_{6.25}\text{Fe}_{0.75}$ and (b) $\text{Pr}_2\text{Co}_6\text{Fe}_1$ compounds annealed at 1023 K. Elemental mapping of $\text{Pr}_2\text{Co}_{6.25}\text{Fe}_{0.75}$: (c) Pr, (d) Co and (e) Fe.

4.3. Structural Analysis of Nanocrystalline $\text{Pr}_2\text{Co}_{7-x}\text{Fe}_x$ Compounds with EXAFS

Figure 3 displays the extended X-ray absorption fine structure (EXAFS) found for the $\text{Pr}_2\text{Co}_{7-x}\text{Fe}_x$ compounds ($x = 0.5, 0.75, \text{ and } 1$). The Fe–K edge is near 7120 eV, with a maximum absorbance located at 7126 eV. The apparent features of the three spectra are similar, revealing that the local structure around the Fe atoms does not change significantly with Fe content. The Fourier transforms (FTs) of the EXAFS data (Figure 3) were calculated between $k_{\min} = 2 \text{ \AA}^{-1}$ and $k_{\max} = 10.5 \text{ \AA}^{-1}$ in order to avoid disturbance and noise. The resolution is $\pi/(2\Delta k) = 0.18 \text{ \AA}$. The main FT peak observed between 1.3 and 3.4 \AA is due to the second atom shell (Pr and Fe) at $\approx 3.0 \text{ \AA}$ and the single Fe–Co scattering at $\approx 2.50 \text{ \AA}$.

Quantitative EXAFS modeling of the local Fe structure in $\text{Pr}_2(\text{Co,Fe})_7$ was initiated with a comprehensive analysis of the five Co sites in Pr_2Co_7 obtained in our previous paper [71]. The first interatomic distances around the central Co/Fe atom are listed in Table 2. The five Co sites were significantly different enough to suggest that a noticeable difference in the corresponding EXAFS spectra was expected; the 4f and 4e sites were almost identical, with a first shell of 6 Co at an average distance of 2.50 \AA and a mixture of 3 Co and 3 Pr at the same distance of around 2.95 \AA in the second shell. Site 2a was similar for the first shell of Co at 2.54 \AA and a second shell composed of 6 Pr at 2.96 \AA . In site 6h, the two first shells contained, respectively, 8 Co around 2.5 \AA and 4 Pr at 3.17 \AA . All four sites were strongly isotropic, and the radial distributions of the first and second distances were rather close. On the other hand, the 12k site was anisotropic with 7 Co first neighbors and a wide radial distribution of Pr second neighbors (3 Pr at 2.91 \AA and 2 Pr at 3.29 \AA).

The five theoretical EXAFS spectra corresponding to the five Fe substitution sites described above were compared to the experimental data. On the qualitative side, we found a better similarity between the 12k model and the experimental results than for the other sites.

Table 2. The interatomic distance (R) and coordination number (N) found with the FEFF6 software package for different possible positions of Fe for the $\text{Pr}_2\text{Co}_{6.5}\text{Fe}_{0.5}$ compound.

| Number | Shell | N | R(Å) |
|----------------------|-------|---|------|
| Fe in-12k | | | |
| 1 | Fe-Co | 7 | 2.50 |
| 2 | Fe-Pr | 3 | 2.91 |
| 3 | Fe-Pr | 2 | 3.29 |
| Fe in 6h-site | | | |
| 1 | Fe-Co | 8 | 2.49 |
| 2 | Fe-Pr | 4 | 3.17 |

To get quantitative results, the adjustment of K-Fe EXAFS spectra was performed using four models that simulated the local structure in the five sites (model 1, model 2, model 3, and model 4 for 12k, 2a, 4f or 4e, and 6h, respectively), which described all of the assumptions of the Fe site according to the results in Table 3. For each shell, we could fit three parameters: the Debye–Waller factor (σ^2), the coordination number (N), which represents the radial distribution function width, and the central atom–neighbor distance (R). We could also make a shift of the energy origin E_0 , but we noticed that this parameter could be fixed in all of our adjustments. To prevent divergence due to the parameters’ correlations [74], we minimized the number of fitted parameters. Therefore, the coordination numbers were fixed for all shells to the values obtained in the crystal structure, and the only amplitude parameters were the Debye–Waller factors. The EXAFS adjustment results are given in Table 3. The Debye–Waller factors increased as a function of x, consistently with the slight decrease in the main peak of the FT amplitude. This was reflective of an increase in structural disorder with substitution disorder. Regarding the neighbor Fe–central atom distances, the Fe-Co distances and the first Fe-Pr distance increased slightly, while the second Fe-Pr distance decreased. As predicted, this Co-Fe substitution effect was mainly due to the increase in Fe-Co bonds with respect to Co-Co bonds.

For all $\text{Pr}_2\text{Co}_{7-x}\text{Fe}_x$ compounds, the model in which Fe atoms occupy the 12k site provides a good adjustment with a QF that is three times smaller than for the other three models. Obviously, the adjustments of the first shell when treating the first Fe-Co contribution at 2.5 Å are similar, and their quality is comparable for the four models. The difference lies in the second shell and is mainly related to the contributions of the unbound Fe-Pr and the second Fe-Co between 2.9 and 3.2 Å. To illustrate the difference between the good adjustment of Model 1 and the other three models, we also show a zoom of their Fourier transforms between 2.3 and 3.5 Å. The improvement in the adjustment of Model 1 over Models 2–4 is depicted quantitatively in the Table 4, in which we determined residuals and quality factors in R space for $\text{Pr}_2\text{Co}_{6.5}\text{Fe}_{0.5}$ for the four models, i.e., in the domain of the full Fourier transform ($\rho\%/QF_R$) or in a restrained R space between 2.3 and 3.5 Å ($QF_{2.3-3.5}$). When the entire R domain is utilized, the model improvement of QF_R is comparable to the values found in k space (Table 3). The significant improvement in the quality factors in the restricted R domain is well established. The good adjustment parameters show that an Fe(12k) atom is enclosed by an average of seven Co neighbors at 2.5 Å, three Pr neighbors at 3.0 Å, and two Pr neighbors at 3.2 Å. In addition, the Debye–Waller factors (σ^2) of the Fe-Pr shell found with Model 2 and Model 3 are about 0.024 \AA^2 , which is physically oversized and unacceptable. The conclusion is that if we attempt to constrain the model to only a second Pr distance, as in all sites, but with 12k, the radial distribution feature of the Pr fitted around Fe attempts to offset this bias with an un-

physical value of the Debye–Waller factor. However, this compensation is not enough to reach a quality of adjustment that is comparable to the value obtained with the assumption of the 12*k* site. Nevertheless, a substitution in a mixture of 12*k*, 6*h*, and 2*a* sites cannot be fully excluded with only the EXAFS adjustment results. We think, however, that the preferential 12*k* substitution is more probable for several reasons described in [69]. Note that the difference between the atomic radii of Co and Fe is only 0.05 Å. Thus, this is not subject to important influences, such as those found in metallic alloys, e.g., Cu–Al, where the observation of Vegard’s law in the long-range mean of the crystal structure versus *x* is significantly different from the locally expanded structure obtained with EXAFS [75]. On the other hand, in the Pr₂Co_{7–*x*}Fe_{*x*} described in this work, we could not find any significant differences between the local structures derived from XRD and EXAFS. Although the substitution disorder was introduced by the partial replacement of Co by Fe, the crystal structure identified through powder diffraction and Rietveld refinement was even verified for the actual crystal cell parameters and atomic positions around the Fe substituent. Nevertheless, XRD did not identify the exact location where the substitution took place, whereas this information was provided by the EXAFS study.

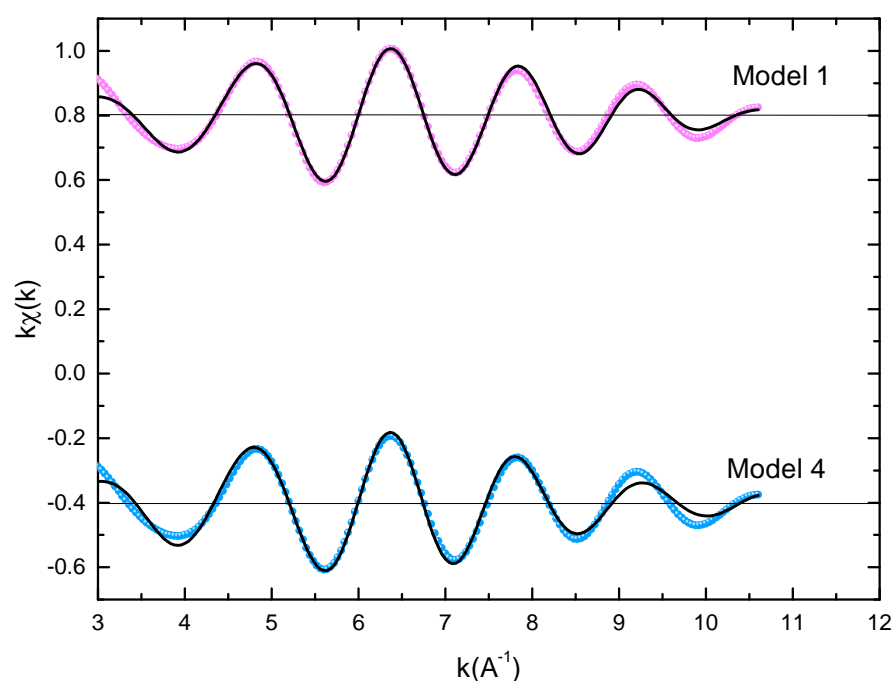


Figure 3. Experimental EXAFS spectra in *k* space of the imaginary part of the Fourier transforms of the Pr₂Co_{6.5}Fe_{0.5} compound, adjusted using Models 1 and 4. Black and red lines show the experimental signal and theoretical curves, respectively.

Table 3. EXAFS adjustment parameters for Pr₂Co_{7–*x*}Fe_{*x*} (*x* = 0.5, 0.75, and 1): interatomic distances (*R*), quality factor (*QF*), and Debye–Waller factor (σ^2).

| | <i>x</i> = 0.5 | | | | <i>x</i> = 0.75 | | | | <i>x</i> = 1 | | | |
|-----------------------------|----------------|------------------------|--------------|-----------|-----------------|------------------------|--------------|-----------|--------------|------------------------|--------------|-----------|
| | <i>N</i> | $\sigma^2(\text{Å}^2)$ | <i>R</i> (Å) | <i>QF</i> | <i>N</i> | $\sigma^2(\text{Å}^2)$ | <i>R</i> (Å) | <i>QF</i> | <i>N</i> | $\sigma^2(\text{Å}^2)$ | <i>R</i> (Å) | <i>QF</i> |
| Model 1 (12<i>k</i>) | | | | | | | | | | | | |
| Fe–Co | 7 | 0.008(1) | 2.48(1) | 0.71 | 7 | 0.010(1) | 2.49(1) | 1.13 | 7 | 0.011(1) | 2.50(1) | 1.21 |
| Fe–Pr | 3 | 0.010(1) | 2.96(2) | | 3 | 0.011(3) | 2.95(2) | | 3 | 0.012(4) | 2.94(3) | |
| Fe–Pr | 2 | 0.010(1) | 3.21(4) | | 2 | 0.011(3) | 3.18(5) | | 2 | 0.012(4) | 3.14(4) | |
| Model 4 (6<i>h</i>) | | | | | | | | | | | | |
| Fe–Co | 8 | 0.010(1) | 2.49(1) | 2.43 | 8 | 0.012(1) | 2.49(1) | 2.65 | 8 | 0.012(1) | 2.49(1) | 3.90 |
| Fe–Pr | 4 | 0.017(6) | 3.01(4) | | 4 | 0.016(4) | 3.02(3) | | 4 | 0.024(3) | 3.04(4) | |

Table 4. Quality factors in R space for the fits of Pr₂Co_{6.5}Fe_{0.5}.

| | ($\rho\%/QF_R$) | ($\rho\%/QF_{2.3-3.5}$) |
|---------|-------------------|---------------------------|
| Model 1 | 1.2/4.9 | 0.18/2.3 |
| Model 4 | 2.91/12.3 | 5.8 / 70.1 |

4.4. Nanocrystalline Pr₂Co₇C_x (x = 0–1) Compounds

Pr₂Co₇C_x compounds have a predominantly hexagonal Ce₂Ni₇ structure with a P6₃/mmc space group. The a and c parameters and the unit cell volume V are increased during C insertion ($\Delta a/a = 0.23\%$, $\Delta c/c = 10.5\%$ and $\Delta V/V = 10\%$). The structural data from the Rietveld analysis are given in Table 5. Figure 4a shows a bright-field micrograph of the Pr₂Co₇C_{0.75} compound. The average grain size Φ_{TEM} is around 150 nm (Figure 4b). The HRTEM images of the nanocrystalline Pr₂Co₇C_{0.75} and Pr₂Co₇C₁ indicate a fully crystallized structure. The compositions of Pr, Co, and C are around 23.2, 74.8, and 2 atomic percent (at.%), respectively.

Table 5. Structural data obtained by the Rietveld analysis of Pr₂Co₇C_x (x = 0.25, 0.50, 0.75, 1) compounds.

| x | 0.0 | 0.25 | 0.5 | 0.75 | 1 |
|--------------------|-----------|-----------|-----------|-----------|-----------|
| a (Å) | 5.068(1) | 5.070(3) | 5.076(1) | 5.079(11) | 5.080(2) |
| c (Å) | 24.456(2) | 24.509(5) | 25.009(3) | 25.576(4) | 26.981(2) |
| c/a | 4.825 | 4.832 | 4.841 | 5.035 | 5.311 |
| V(Å ³) | 544.02 | 547 | 555 | 567.4 | 598.9 |
| R _B | 3.1 | 2.43 | 1.31 | 2.76 | 2.42 |
| χ^2 | 3.80 | 3.28 | 3.60 | 3.38 | 3.36 |

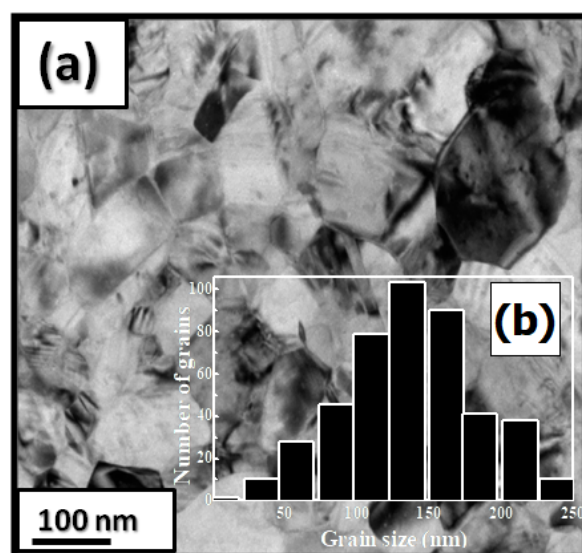
**Figure 4.** Bright-field micrographs of Pr₂Co₇C_{0.75} (a). The grain size distribution is shown in the inset (b).

Figure 5a shows the grain morphology of the nanocrystalline Pr₂Co₇C_{0.75} compound when analyzed with TEM. The nanocrystalline Pr₂Co₇C_{0.75} compound is composed of larger grains of about 150 nm. By zooming in on the area between these grains (Figure 5b), a different phase consisting of very small grains of about 7–12 nm is found. The corresponding EDX analysis is presented in Figure 5c, which depicts the intensity distribution profiles of the Pr, Co, and C elements. The purple line corresponds to the profile of Co, and the red line corresponds to Pr. C is represented by a blue line. The slightly decreased

intensity distribution profiles of Pr and C in the area between the grains indicate a more Co-rich phase.

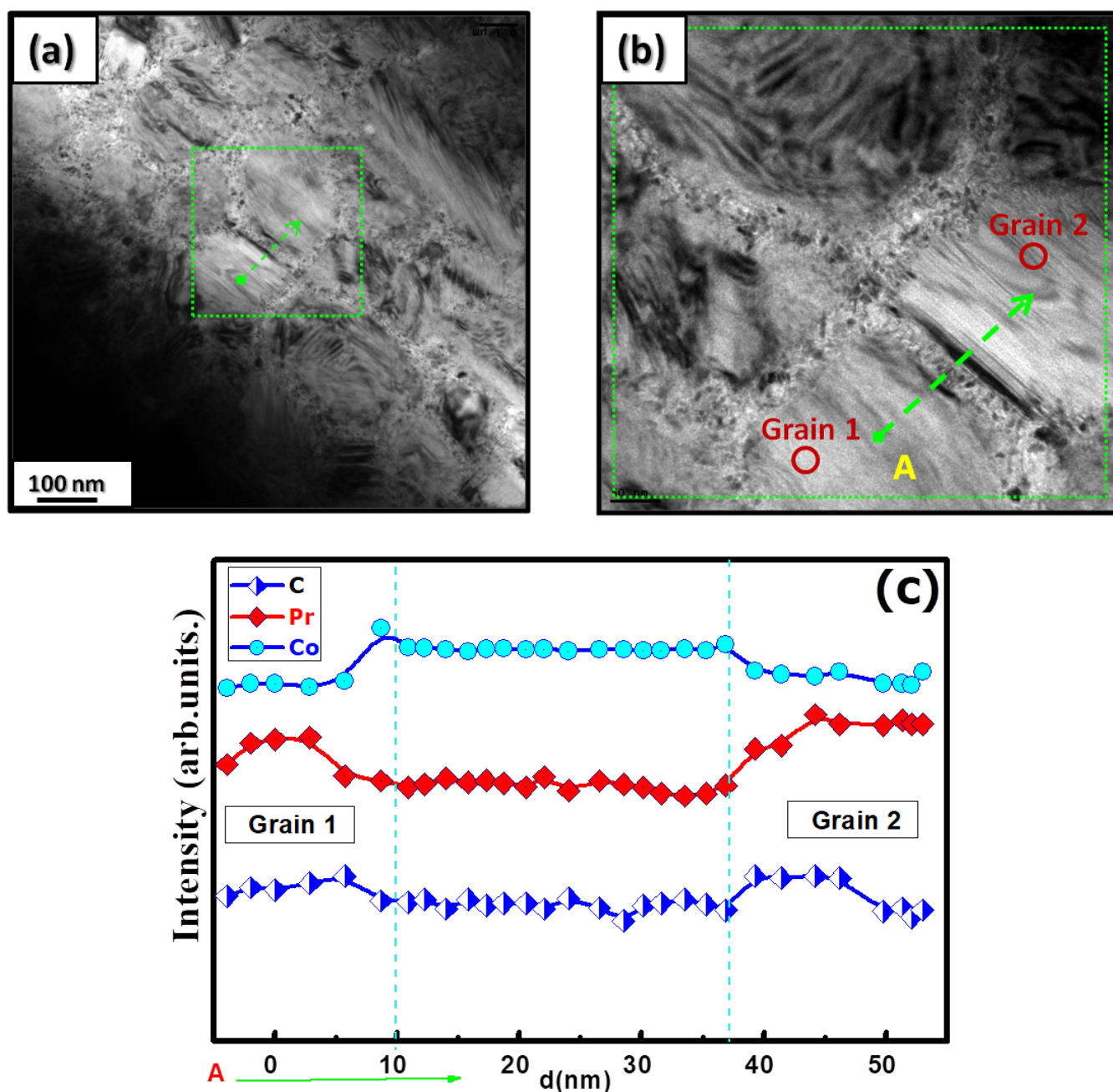


Figure 5. (a) Bright-field TEM image of the nanocrystalline $\text{Pr}_2\text{Co}_7\text{C}_{0.75}$ compound. (b) High-resolution image of the area in between grains shown in the green square in (a). (c) The EDS line profile presented as a function of the distance d from point A.

4.5. Nanocrystalline $\text{Pr}_2\text{Co}_7\text{H}_x$ ($x = 0\text{--}10.8$) Compounds

We investigated the hydrogen absorption–desorption properties of the Pr_2Co_7 compound along the P–C isotherm. The P–C isotherm curves at $T = 313$ K are displayed in Figure 6. Two plateaus were clearly seen. These results indicate the presence of three distinct crystallographic hydrides, which can be defined as follows: α , β , and γ . The α phase is the solid solution phase based on Pr_2Co_7 ($y \leq 0.42$), followed by the β phase ($0.61 < y \leq 0.72$), and γ is the phase with the highest H content ($y \leq 1.05$). The 1st plateau pressures were around 0.012×10^6 Pa (absorption) and 0.005×10^6 Pa (desorp-

tion). The 2nd plateau pressures were at approximately 0.032×10^6 Pa (absorption) and 0.013×10^6 Pa (desorption). The maximum H storage content was $y = 1.2$ H/M in the 1st absorption, and about 60% of the maximum H content stayed after the 1st desorption. The y (H/M) content is the ratio of H atoms x (H/f.u) to all metal atoms ($y = x/9$). The crystal structure of the Pr_2Co_7 compound transformed from hexagonal ($P6_3/mmc$ space group, α phase) to orthorhombic ($Pbcn$ space group, β phase) and monoclinic ($C2/c$ space group, γ phase) phases during hydrogenation. These two phases were recognized as $\text{Pr}_2\text{Co}_7\text{H}_{6.1}$ and $\text{Pr}_2\text{Co}_7\text{H}_{10.8}$. Their enthalpies, ΔH , were estimated to be -48.8 and -49.9 kJ/mol. H_2 , respectively, from the Van 't Hoff plot. The hydrogenation mechanism can be described as follows:

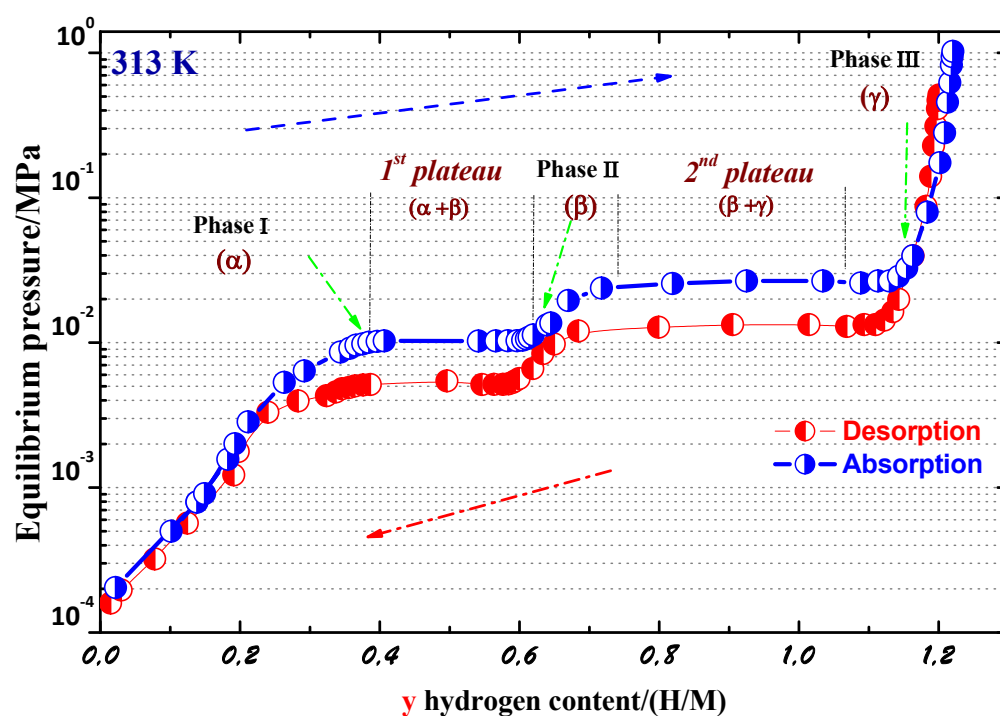
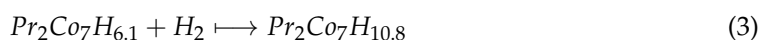
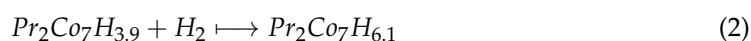
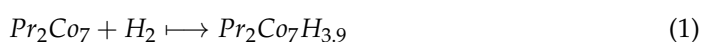


Figure 6. P–C isotherm curves of the Pr_2Co_7 compound at 313 K.

The structural parameters of $\text{Pr}_2\text{Co}_7\text{H}_{6.1}$ (β phase) and $\text{Pr}_2\text{Co}_7\text{H}_{10.8}$ (γ phase) were, respectively, $a = 5.070$ Å, $b = 8.153$ Å, $c = 28.978$ Å and $a = 5.268$ Å, $b = 7.103$ Å, $c = 31.498$ Å, $\beta = 90.17^\circ$. The average grain sizes Φ were 170 and 185 nm for $x = 6.1$ and 10.8, respectively. As indicated in Figure 7, the deviation induced the displacement of the Co_1 (2a) atoms on the (001) plane by as much 0.19 Å from the corresponding position in the orthorhombic structure due to the large lattice parameter c , which was more than 30 Å. The orthorhombic unit cell can be viewed in relation to a hexagonal cell, where the a , b , and c parameters of the two structures are related to each other as $a_{\text{orth}} = a_{\text{hex}}$, $b_{\text{orth}} = 2\cos\alpha a_{\text{hex}}$ ($\alpha = 30^\circ$), and $c_{\text{orth}} = c_{\text{hex}}$. An orthorhombic $Pbcn$ model has the closest structure to that of the $C2/c$ model [57,63,76].

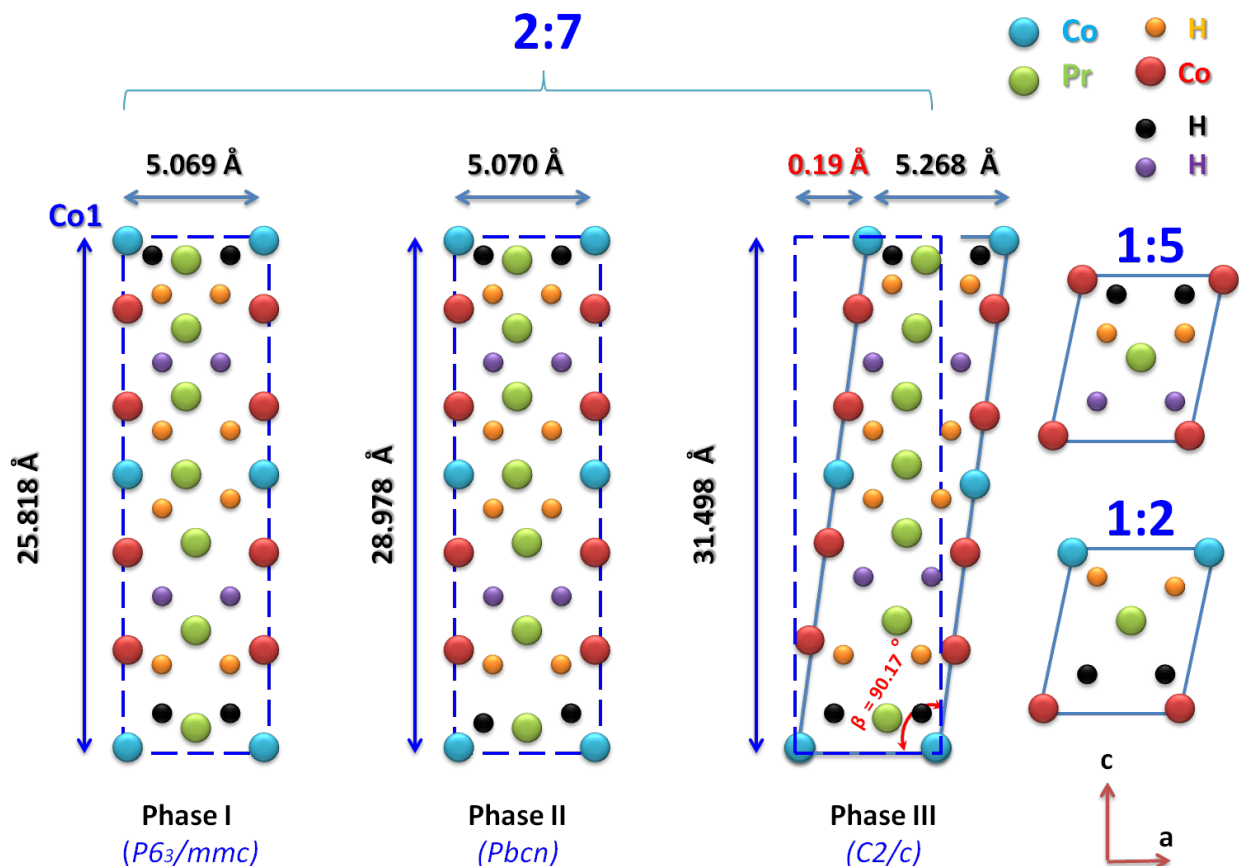


Figure 7. Position of the Co_1 atom in the orthorhombic ($Pbcn$) and monoclinic ($C2/c$) structures projected in the $\langle 1\ 0\ 1 \rangle$ direction.

5. Intrinsic Magnetic Properties

5.1. Nanocrystalline $\text{Pr}_2\text{Co}_{7-x}\text{Fe}_x$ ($x = 0, 0.25, 0.5, 0.75,$ and 1) Compounds

To study the effects of Co substitution by Fe on the intrinsic magnetic properties of the alloy samples, the Curie temperature T_C for the nanocrystalline $\text{Pr}_2\text{Co}_{7-x}\text{Fe}_x$ phase was measured for each Fe content x . The nanocrystalline $\text{Pr}_2\text{Co}_{7-x}\text{Fe}_x$ compounds were ferromagnetic. The T_C value increased from 600 K for the nanocrystalline Pr_2Co_7 compound, attaining a maximum of 760 K at $x = 0.5$, and then decreased for $x = 0.75$ and $x = 1$. The T_C values were around 695 and 667 K, respectively. The T_C value was the result of two effects: the electronic effect related to the filling of the $3d$ band of Fe atoms and the magnetovolume effect related to the Co-Co distances [71]. The $M(H)$ curves of the nanocrystalline $\text{Pr}_2\text{Co}_{7-x}\text{Fe}_x$ compounds were measured at 293 K. The determination of M_S was performed using the law of approach to saturation [77]:

$$M(H) = M_S + a/H^2 \quad (4)$$

The M_S values were converted into the magnetic moment per formula unit μ_s . The μ_s increased linearly with increasing the Fe content x . The theoretical equation of μ_s as a function of x was defined by the formula: $\mu_s = \mu(x = 0) + 7x$ ($0 \leq x \leq 1$), where $\mu(x = 0)$ is the saturation moment of the Pr_2Co_7 compound (in $\mu_B/\text{f.u.}$). The experimental data corresponded well to the theoretical forecast. The evolution of μ_s with x could be justified by the reduction in the average number of $3d$ electrons when replacing the Co atoms with Fe, which led to a progressive strengthening of the Co($3d$)-Co($3d$) exchange interactions and, thus, to an enhanced magnetic moment with the $3d$ [71]. We realized the XRD patterns of $\text{Pr}_2\text{Co}_{7-x}\text{Fe}_x$ powders that were magnetically aligned at $T = 293$ K in a field of 0.5 T. For samples with $x < 0.5$, the (001) reflections were heavily enhanced, indicating EMD along

the c axis. For $x > 0.5$, the diagram shows a lower intensity of the (001) peaks, while the reflections (h0l) are reinforced, implying that the EMD of the $\text{Pr}_2\text{Co}_{7-x}\text{Fe}_x$ sample deviates from the c axis.

5.2. Nanocrystalline $\text{Pr}_2\text{Co}_7\text{C}_x$ ($x = 0-1$) Compounds

The Curie temperature T_C of the Pr_2Co_7 compounds was determined according to the Co-Co, Pr-Co, and Pr-Pr interactions. In general, the Co-Co interaction was dominant, and the Pr-Co and Pr-Pr interactions were negligible. From the obtained structural data, the C insertion led to a change in the a , c parameters of the Pr_2Co_7 compound and thus to an increase in the unit cell volume V of 2.5%. The a , c parameters varied from $a = 5.068 \text{ \AA}$ and $c = 24.457 \text{ \AA}$ for Pr_2Co_7 to $a = 5.080 \text{ \AA}$ and $c = 26.980 \text{ \AA}$ for $\text{Pr}_2\text{Co}_7\text{C}$. Consequently, the Co(12k)-Co(12k), Co(12k)-Co(4f), and Co(4f)-Co(4f) distances increased the related $J_{12k-12k}$, J_{12k-4f} , and J_{4f-4f} exchange interactions. As a result, the T_C increased due to the magnetovolume effect. Figure 8 gives the influence of C insertion on T_C . T_C increased from 600 to 740 K for $x = 1$, which corresponds to an increase of 23.5%.

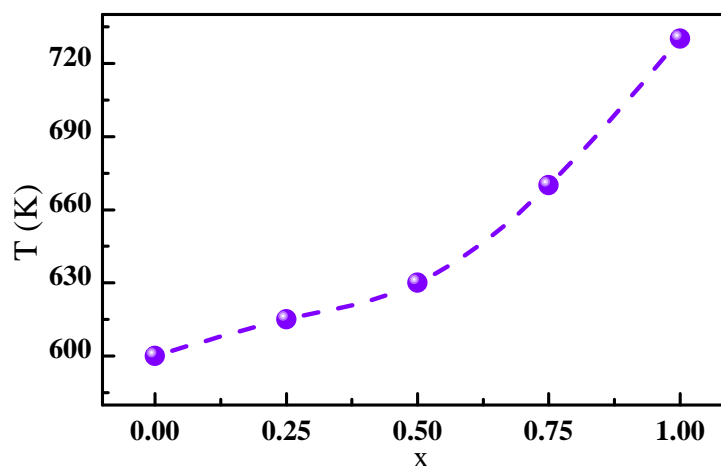


Figure 8. Evolution of the Curie temperature T_C as a function of the C content.

The magnetization measurements, $M(H)$, which were performed up to 90 kOe, indicated that the saturation process was hardly achievable at $T = 293 \text{ K}$. This was due to the presence of an important magnetocrystalline anisotropy. An insertion content $x = 1$ in the $\text{Pr}_2\text{Co}_7\text{C}_x$ system induced an important increase in the magnetization compared to Pr_2Co_7 , but it did not change the type of magnetic behavior, which always remained ferromagnetic. The M_s values of the $\text{Pr}_2\text{Co}_7\text{C}_x$ compounds were determined from the $M(H)$ curves. The dependence of M_s on the C insertion content in $\text{Pr}_2\text{Co}_7\text{C}_x$ showed a linear behavior at 293 K. The insertion of a small content of C caused an increase in M_s from 8.2 for $x = 0$ to $11.6 \mu_B/\text{f.u}$ for 1, corresponding to an increase of about 34%.

5.3. Nanocrystalline $\text{Pr}_2\text{Co}_7\text{H}_x$ ($x = 0-10.8$) Hydrides

The H absorption resulted in a variation of the lattice parameters of the Pr_2Co_7 compound and, therefore, an increase in the cell volume V . The nearest-neighbor number of each Co atom and the Co-Co distances were then determined depending on the H content. The Co-Co distances most influenced by H absorption were those involving the Co₃ and Co₅ atoms, respectively, in the 4f and 12k sites. Therefore, the increase in the Co₅-Co₅, Co₃-Co₅, and Co₃-Co₃ distances led to a modification of the exchange interactions J_{ij} , which had some impact on the increase in T_C . T_C increased as a function of H content from 600 K at $x = 0$ to 691 K at $x = 3.75$, then decreased for $x > 3.75$. The $\text{Pr}_2\text{Co}_7\text{H}_x$ hydrides presented a ferromagnetic compartment for all H contents. The XRD patterns of the magnetically aligned $\text{Pr}_2\text{Co}_7\text{H}_x$ hydride powder samples showed only (0 0 l)-type peaks, implying that the EMDs of $\text{Pr}_2\text{Co}_7\text{H}_x$ hydrides were along the c axis.

5.4. Mean Field Theory (MFT) and Random Magnetic Anisotropy (RMA) Analysis

5.4.1. Nanocrystalline $\text{Pr}_2\text{Co}_7\text{C}_x$ ($x = 0-1$) Compounds

The ferromagnetic alignment of the magnetic moments of Pr and Co atoms, M_{Pr} and M_{Co} , can be described using the following expression:

$$M = M_{Co} + M_{Pr} \quad (5)$$

M_{Pr} and M_{Co} were estimated using mean field theory (MFT). The magnetization M can be determined using expression (5). M_{Co} and M_{Pr} were expected to follow the Brillouin functions [78]. $M(T)$ was fitted for different C contents x . The experimental data align well with the theoretical curves. T_C was found to be in agreement with the experimentally derived temperature. M_{Pr} , M_{Co} , and M were also determined for $\text{Pr}_2\text{Co}_7\text{C}_{0.25}$ (Figure 9a). The J_{Co-Co} and J_{Co-Pr} exchange interactions increased as a function of x , while J_{Pr-Pr} was found to be constant around $2 \cdot 10^{-23}$ J. Inserting C into the Pr_2Co_7 induced an enhancement of T_C from 600 to 730 K when x was increased from 0 to 1 (Figure 9b). The increase in T_C can be ascribed to electronic and magnetovolumic effects.

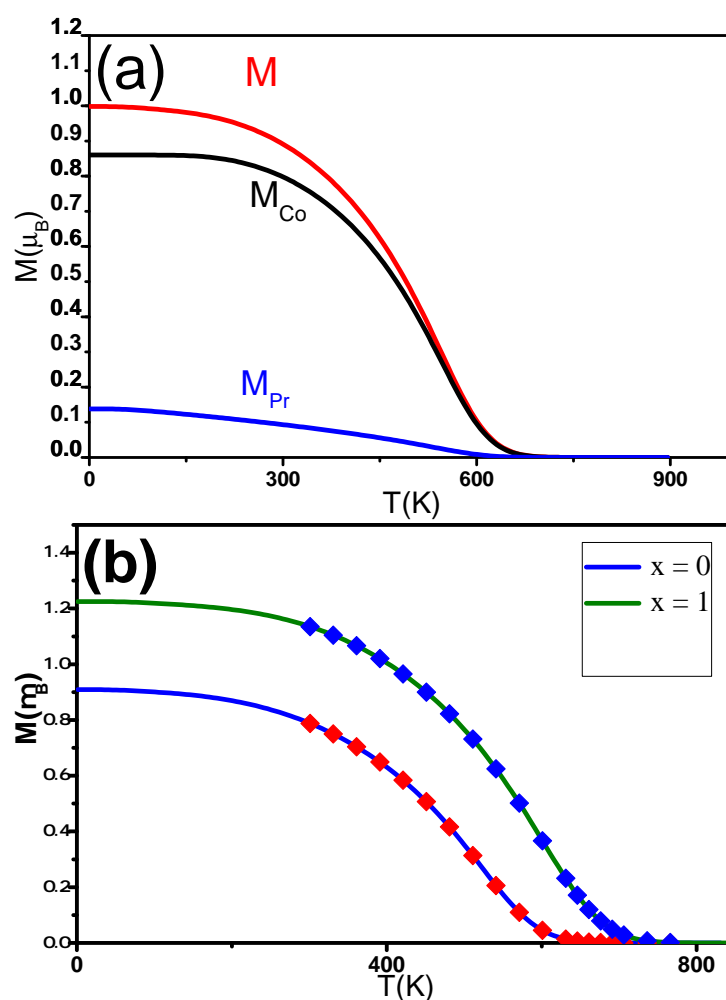


Figure 9. (a) Calculated change in the magnetic moments ($M_{Pr}(T)$, $M_{Co}(T)$) and magnetization ($M(T)$) of the nanocrystalline $\text{Pr}_2\text{Co}_7\text{C}_{0.25}$ compound. (b) The solid lines are the $M(T)$ of nanocrystalline $\text{Pr}_2\text{Co}_7\text{C}_x$ found calculated in the MFT analysis. The symbols show the experimental data.

The magnetization curves $M(H)$ of the nanocrystalline $\text{Pr}_2\text{Co}_7\text{C}_x$ compounds are displayed in Figure 10. Based on the law of approach to saturation, which describes the $M(H)$ for $H \gg H_c$, M close to the M_s can be estimated by:

$$M(H) = M_s \left(1 - \frac{\sigma}{(H + H_u + H_{ex})^{1/2}} + \frac{\rho}{(H + H_u + H_{ex})^2} \right) + \chi H \quad (6)$$

H , H_{ex} , and H_u correspond to the applied magnetic field, the exchange field, and the coherent anisotropy field, respectively. χ is the magnetic susceptibility. σ and ρ are constants. Figure 10 displays the $M(H)$ curves near saturation for the $\text{Pr}_2\text{Co}_7\text{C}_x$ compounds. As illustrated in Figure 10, Equation (6) fits the experimental data well. From the fits of Equation (6), we extracted the anisotropy field H_a , exchange field H_{ex} , and the exchange constant A_{ex} , which are mentioned in Table 6. The σ and ρ parameters are correlated to H_a and H_{ex} with the following expressions [57]:

$$\sigma = \frac{H_a^2}{15H_{ex}^{3/2}} = \rho H_{ex}^{-3/2} = \rho \left(\frac{2A_{ex}}{M_s d_c^2} \right)^{-3/2} \quad (7)$$

The anisotropy field $H_a = 2K_1/M_s$. K_1 is the constant anisotropy.

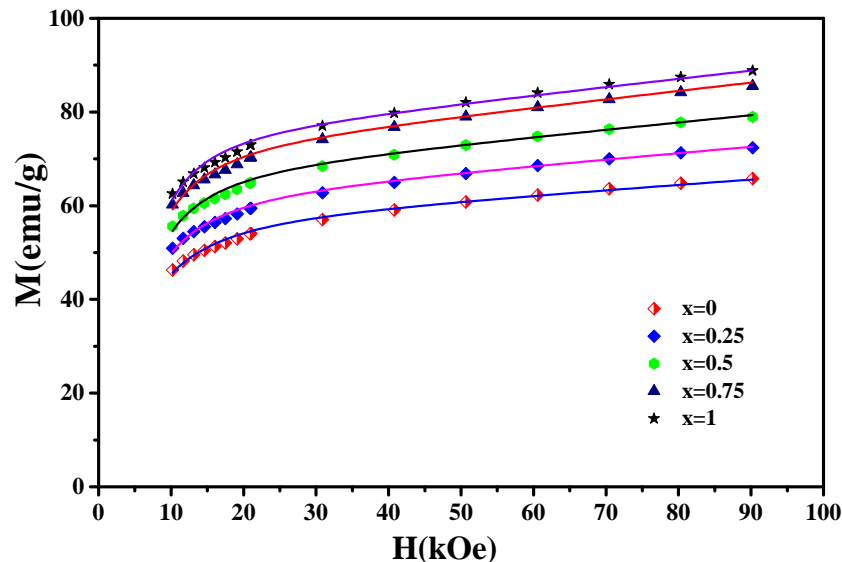


Figure 10. The magnetization curves $M(H)$ of the nanocrystalline $\text{Pr}_2\text{Co}_7\text{C}_x$ compounds ($x = 0, 0.25, 0.5, 0.75, \text{ and } 1$). The solid lines show the fit to the experimental data (symbols).

d_c is the distance over which the local anisotropy axis is related. The d_c values were estimated with statistical correlation magnetometry. The parameter λ plays an important role in the distinction between weak anisotropy ($\lambda < 1$) and strong anisotropy ($\lambda > 1$). It was found using the following formula [58]:

$$\lambda = (2/15)^{1/2} (H_a/H_{ex}) \quad (8)$$

For all C contents, λ was higher than 1, which is consistent with a ferromagnetic system with strong random anisotropy.

Table 6. The values of M_s , the factors σ and ρ , the field H_a (kOe), H_u (kOe), H_{ex} (kOe), A_{ex} , and d_c (nm) for the nanocrystalline $\text{Pr}_2\text{Co}_7\text{C}_x$ ($x = 0, 0.25, 0.5, 0.75, 1$) compounds, measured at 293 K.

| δ | M_s | σ | ρ | H_a | H_u | H_{ex} | A_{ex} | d_c |
|----------|-------|----------|--------|--------|--------|----------|----------|-------|
| 0 | 55 | 3450 | 12.5 | 227.48 | −37.12 | 42.39 | 1.15 | 15 |
| 0.25 | 60 | 3000 | 9 | 212.13 | −43.38 | 48.07 | 1.81 | 22 |
| 0.50 | 65 | 2600 | 8 | 197.48 | −44.17 | 47.27 | 2.05 | 35 |
| 0.75 | 70 | 2300 | 7 | 185.74 | −45.25 | 47.61 | 2.57 | 60 |
| 1 | 73 | 1900 | 5 | 168.81 | −51.41 | 52.46 | 3.04 | 134 |

5.4.2. Nanocrystalline $\text{Pr}_2\text{Co}_7\text{H}_x$ ($x = 0$ –10.8) Hydrides

The exchange interactions of nanocrystalline $\text{Pr}_2\text{Co}_7\text{H}_x$ were calculated as a function of H content using the MFT (Table 7). $J_{\text{Co-Co}}$ and $J_{\text{Co-Pr}}$ increased when the H content increased. The exchange interaction $J_{\text{Pr-Pr}}$ was around 2×10^{-23} J. $M_{\text{Pr}}(T)$, $M_{\text{Co}}(T)$, and $M(T)$ were fitted. The T_C values were found to be in good agreement with the experimentally determined values. T_C increased as a function of H content from 600 K at $x = 0$ to 691 K at $x = 3.75$, dealing with an increase of about 9.1%, then decreasing for $x > 3.75$. The peak value appearance of T_C at $x = 3.75$ resulted from the H content dependence of the exchange interaction parameter of $J_{\text{Co-Co}}$. The enhancement of the T_C of $\text{Pr}_2\text{Co}_7\text{H}_x$ hydrides for $x \leq 3.75$ could be the result of two effects: the electronic effect associated with a decrease in the hybridization of Co(3d) atoms with their neighbors and the magnetovolume effect associated with Co-Co distances, which suggests a decrease in antiferromagnetic interaction [57]. The Co-Co exchange interactions increased from 166×10^{-23} J for $x = 0$ to 178×10^{-23} J for $x = 3.75$. The decrease in T_C for $x > 3.75$ was mostly due to the reduction in Co-Co exchange interactions from 178×10^{-23} to 130×10^{-23} J for $x = 10.8$.

Table 7. The saturation magnetization M_s , factors σ and ρ , magnetic anisotropy field H_a (kOe), coherent anisotropy field H_u (kOe), exchange field H_{ex} (kOe), exchange constant A_{ex} , and distance d_c (nm) values for the nanocrystalline $\text{Pr}_2\text{Co}_7\text{H}_x$ hydrides, measured at 293 K.

| δ | M_s | σ | ρ | H_a | H_u | H_{ex} | A_{ex} | d_c |
|----------|-------|----------|--------|--------|--------|----------|----------|-------|
| 0 | 55 | 3450 | 12.5 | 227.48 | −3.712 | 42.39 | 1.15 | 15 |
| 0.25 | 65 | 2500 | 9 | 212.13 | −4.009 | 48.07 | 1.45 | 21 |
| 2.50 | 77 | 3100 | 8.92 | 197.48 | −4.817 | 47.27 | 2.04 | 31 |
| 3.75 | 74 | 2200 | 6.91 | 197.48 | −5.122 | 47.27 | 2.05 | 33 |
| 6.10 | 70.63 | 2108 | 6.02 | 185.74 | −5.253 | 47.61 | 2.56 | 56 |
| 10.8 | 56.57 | 1957 | 5.23 | 168.81 | −5.495 | 52.46 | 3.07 | 112 |

From the fits of Equation (6), we also determined the different magnetic parameters, which are enumerated in Table 7. H_a varied from 130 to 150 kOe. The constant anisotropy K_1 and μ_{Co} increased from 5.24×10^7 to 5.69×10^7 erg/cm³ and from 1.01 to 1.37 μ_B , respectively, then decreased for $x > 2.5$. The decrease in K_1 was well related to the decrease in μ_{Co} using the relation $K_1 \propto m^3$ (m is relative change in magnetization). This agrees with the statement that the magnetization μ_s for the $\text{Pr}_2\text{Co}_7\text{H}_x$ hydrides is principally due to the Co moment μ_{Co} . μ_s increased from 8.32 at $x = 0$ to 14 μ_B /f.u. at $x = 2.5$, then decreased for $x > 2.5$. The decrease in μ_s was due to the reduced hybridization state between the 3d(Co) and 5d(Pr) bands engendered by the volume expansion, which led to a decrease in the state density at the Fermi level. The 3d(Co) bands became closer and, therefore, more localized. Hence, the magnetic moment per Co atom increased with the H atom absorption in a first step. This created new Co-H bonds, which resulted in a decrease in the magnetization of the $\text{Pr}_2\text{Co}_7\text{H}_x$ hydrides, which confirms the hypothesis on the electronic

and magnetovolumic effects of H absorption [57,58]. The coercivity H_c can be defined by the random anisotropy model [79]. H_c can be written with the following expression:

$$H_c = \alpha(A_{ex}K_1)^{1/2}/\Phi M_s = \alpha\zeta/\Phi M_s \quad (9)$$

where Φ is the grain size.

As shown in Figure 11, the experimental values of H_c as a function of ζ and H_c fit well and linearly with ζ . The α parameter was estimated to be about 6.91. The values of H_c obtained from (9) are in agreement with the experimental values.

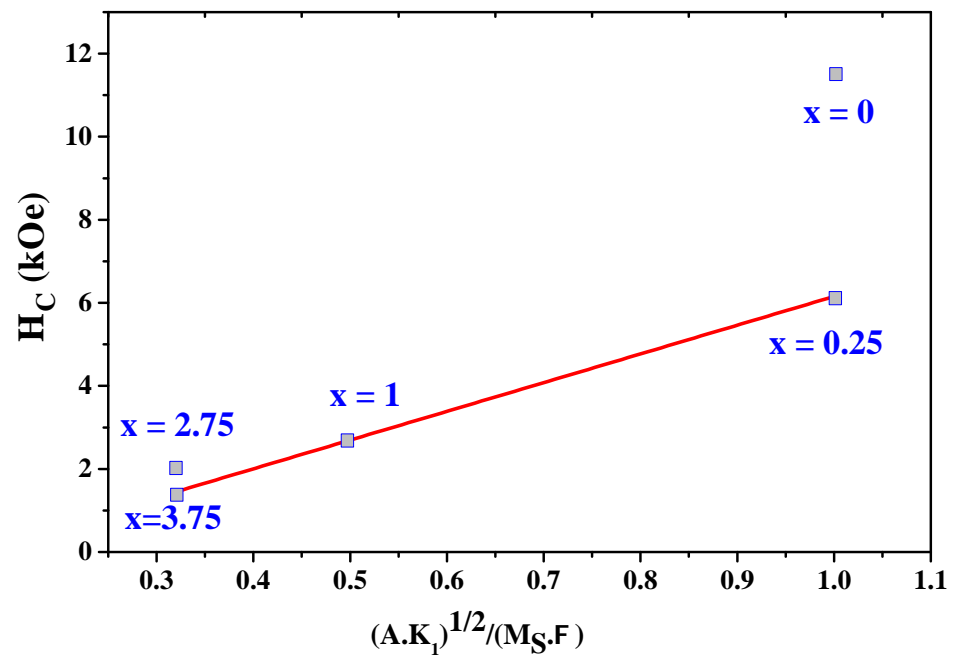


Figure 11. The experimental data on the coercivity H_c as a function of $\zeta = (AK_1)^{1/2}$.

5.5. Magnetocaloric Effect of the Nanocrystalline Pr_2Co_7 Compound

The measurements of the $M(H)$ curves were carried out around the Curie temperature T_C going from 562 to 598 K for 2:7 (R) and from 585 to 615 K for 2:7 (H). The same type of magnetization behavior as for Pr_2Co_7 could be observed. On the other hand, when $T > T_C$, the Pr_2Co_7 compound was paramagnetic, and its magnetization increased gradually with the applied field. The magnetization increased rapidly with the applied field until saturation was achieved. It should be noticed that, for the 2:7 R structure, saturation was not achieved compared to the 2:7 H structure; this was related to the presence of strong uniaxial anisotropy in this compound. We traced the Arrott curves $M^2 = f(\mu_0 H/M)$ for the Pr_2Co_7 compound in its 2:7 H and 2:7 R structures based on the $M(H)$ isotherms found. It should be remarked that these curves showed a positive slope; this confirmed that the Pr_2Co_7 compound for the two structures had a second-order phase transition from the paramagnetic to the ferromagnetic state [80].

We calculated the evolution of the magnetic entropy ΔS_M as a function of temperature T and applied field H . Figures 12 and 13 show the thermal variations in the changes in magnetic entropy for the 2:7 H and 2:7 R structures, respectively. The $-\Delta S_M^{\max}$ of the 2:7 R structure was greater than that for the 2:7 H structure. As shown in Figure 13, the maximum value was about 3.7 J/(kg.K) under a magnetic field of 0–15 kOe. There were two important contributions to the maximum change in magnetic entropy ΔS_M : the M_s and $\Delta M_T(H)$, which was the difference between two successive isotherms at a particular magnetic field around the temperature T_C . The peak that corresponded to ΔS_M became a plateau starting at T_C . This transition from a single peak to a plateau was seen for the first time for a second-order magnetic transition. The relative cooling power (RCP) values were 102.7 and

8.5 J/kg, respectively, for the 2:7 R and 2:7 H structures. The calculation was based on the variation of ΔS_M according to the equation: $RCP = -\Delta S_M \delta T_{FWHM}$ [8], where ΔS_M and δT_{FWHM} are the maximum of the entropy variation and the full width at half maximum of the temperature dependence of the change in magnetic entropy ΔS_M .

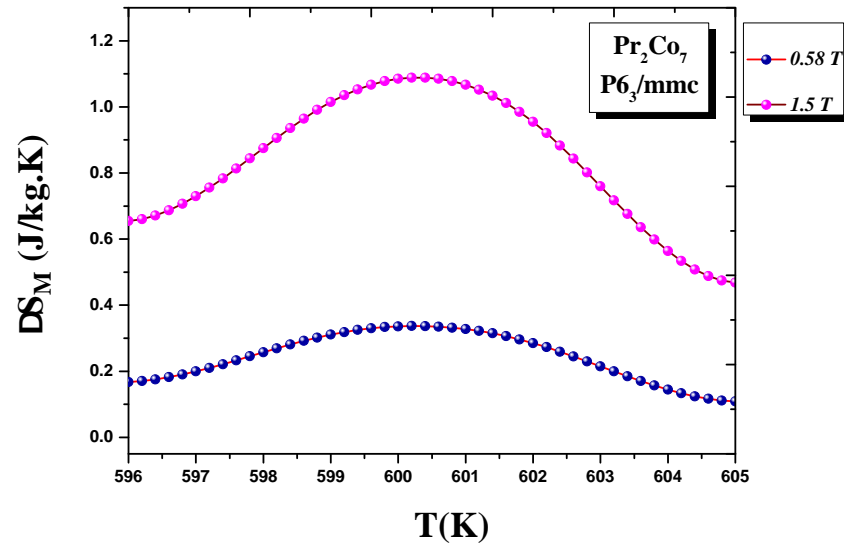


Figure 12. Magnetic entropy $\Delta S_M(T)$ around the Curie temperature T_C for the 2:7 H structure.

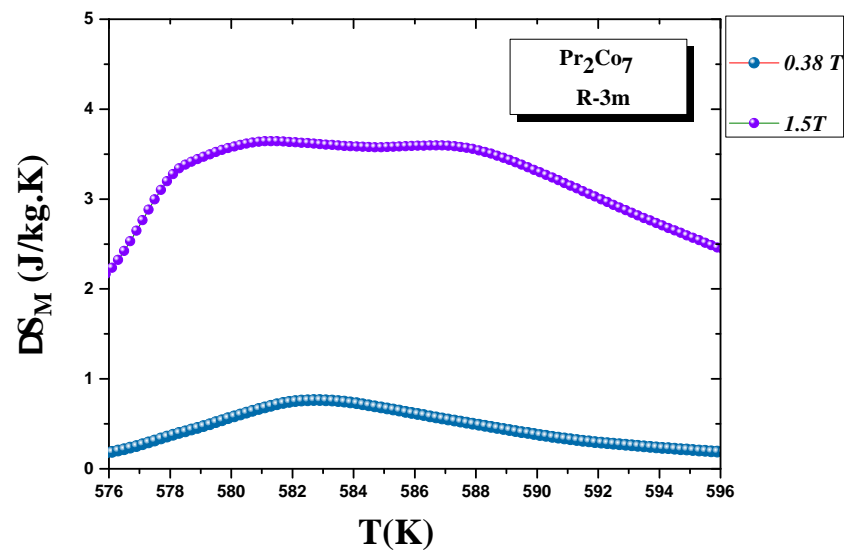


Figure 13. Magnetic entropy $\Delta S_M(T)$ around the Curie temperature T_C for the 2:7 R structure.

6. Extrinsic Magnetic Properties

6.1. Nanocrystalline $Pr_2Co_{7-x}Fe_x$ ($x = 0, 0.25, 0.5, 0.75, \text{ and } 1$) Compounds

To obtain a nanocrystalline state with excellent extrinsic magnetic properties, annealing was performed at different temperatures. At each annealing temperature T_a , the hysteresis loops were measured. The evolution of H_c as a function of T_a initially exhibited a characteristic increase in H_c with T_a up to a maximum H_c value, which was followed by a decrease in H_c at higher temperatures of $T_a > 973$ K. The most favorable microstructure for optimal magnetic properties corresponded to T_a between 973 and 1073 K. The highest H_c obtained for the nanocrystalline $Pr_2Co_{6.5}Fe_{0.5}$ and $Pr_2Co_{6.75}Fe_{0.25}$ compounds was $H_c = 11.5$ kOe and $H_c = 12$ kOe, respectively. The respective values of remanent magnetization M_r were 43 and $M_r = 48$ emu/g. The decrease in H_c could mainly be due to the decrease in magnetocrystalline anisotropy after the substitution. H_c depended principally

on the magnetocrystalline anisotropy H_a . The substitution of Co by Fe implied a reduction of the contribution of the $3d$ axial and, thus, a decrease in H_c as a function of x , as has been shown by X-ray diffraction in oriented powders [71]. We studied the evolution of $(BH)_{\max}$. The $(BH)_{\max}$ value increased with T_a and then decreases when T_a increased for all values of Fe content x . Table 8 summarizes the H_c , M_r , and $(BH)_{\max}$ values as a function of content x . The nanocrystalline $\text{Pr}_2\text{Co}_{6.5}\text{Fe}_{0.5}$ compound annealed at 973 K can currently be useful for applications in the field of permanent magnets.

Table 8. Extrinsic magnetic properties of $\text{Pr}_2\text{Co}_{7-x}\text{Fe}_x$ at $T = 293$ K: H_c (kOe), M_r (emu/g), and $(BH)_{\max}$ (MGOe).

| x | H_c | M_r | $(BH)_{\max}$ |
|------|-------|-------|---------------|
| 0.25 | 12 | 48 | 9.1 |
| 0.5 | 11.5 | 43 | 9 |
| 0.75 | 6.5 | 41 | 5.5 |
| 1.00 | 2 | 40 | 1.3 |

6.2. Nanocrystalline $\text{Pr}_2\text{Co}_7\text{C}_x$ ($x = 0-1$) Compounds

Figure 14 shows the hysteresis loops of the Pr_2Co_7 , $\text{Pr}_2\text{Co}_7\text{C}_{0.25}$, and $\text{Pr}_2\text{Co}_7\text{C}_{0.75}$ compounds annealed at 1073 K and measured at 293 K. The hysteresis loops show that these compounds are isotropic and confirm that they have only one ferromagnetic phase. We present in Figure 15 the evolution of H_c as a function of annealing temperature T_a for the $\text{Pr}_2\text{Co}_7\text{C}_x$ compounds. The curve passes through a maximum for $T_a = 1073$ K. Two regions are thus highlighted; they are correlated to the mean grain size and the defects. The H_c increases with T_a in the lattice with the 2:7 H structure, i.e., with the grain size and the reduction of the defects, until the critical value found at 1073 K. The grains get bigger and H_c decreases. We give in Table 9 the evolution of H_c , M_r , and $(BH)_{\max}$ as a function of x . The decrease in H_c is mainly due to the decrease in magnetocrystalline anisotropy H_a and the grain size, which becomes larger during C insertion (Figure 15). The best properties found were recorded for the the $\text{Pr}_2\text{Co}_7\text{C}_{0.25}$ compound that was annealed at 1075 K; the H_c value was equal to 17.5 kOe with an M_r of 43 emu/g, an M_r/M_s ratio of 0.60, and $(BH)_{\max} = 12.5$ MGOe.

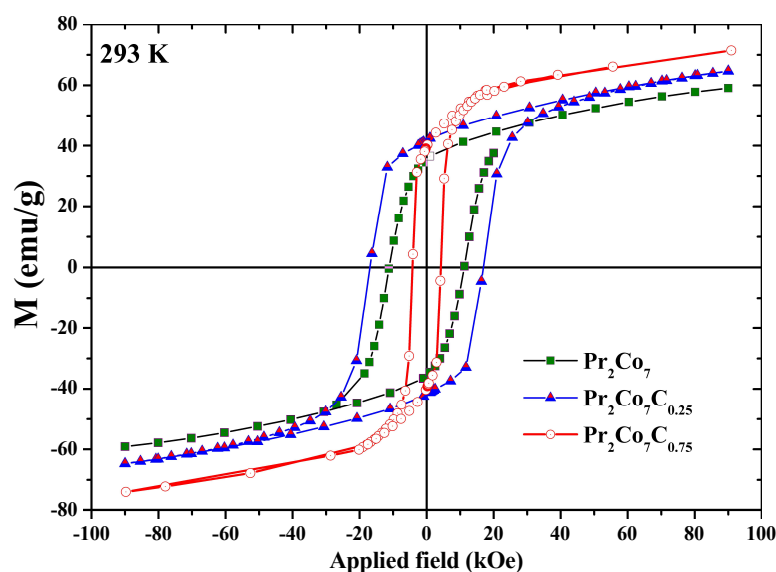


Figure 14. Hysteresis loops of the Pr_2Co_7 , $\text{Pr}_2\text{Co}_7\text{C}_{0.25}$, and $\text{Pr}_2\text{Co}_7\text{C}_{0.75}$ compounds, measured at 293 K.

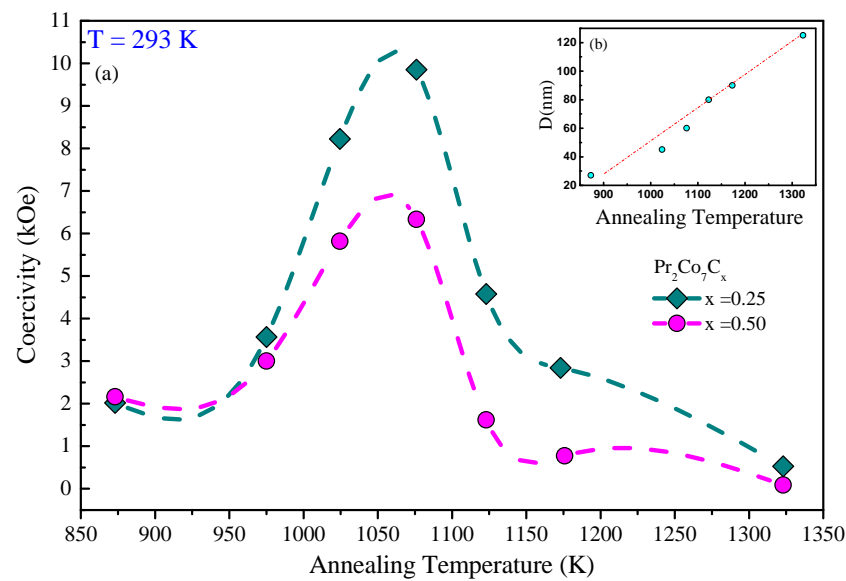


Figure 15. (a) The evolution of the coercivity H_c as a function of annealing temperature T_a of the $\text{Pr}_2\text{Co}_7\text{C}_x$ compounds ($x = 0, 0.25$). (b) The grain size as a function of C content x is shown in the inset.

Table 9. Magnetic properties of $\text{Pr}_2\text{Co}_7\text{C}_x$ compounds at $T = 293$ K.

| x | 0 | 0.25 | 0.50 | 0.75 | 1 |
|-----------------------------------|------|------|------|------|------|
| H_c (kOe) | 11 | 17.5 | 6.1 | 1.5 | 0.95 |
| M_r (emu/g) | 36 | 43 | 41 | 41 | 40 |
| $(\text{BH})_{\text{max}}$ (MGOe) | 11.8 | 12.5 | 5.3 | 3.1 | 1.1 |

6.3. Nanocrystalline $\text{Pr}_2\text{Co}_7\text{H}_x$ ($x = 0-10.8$) Hydrides

The demagnetization curves found in the hysteresis loops of the $\text{Pr}_2\text{Co}_7\text{H}_x$ hydrides ($x = 0.25, 6.1, \text{ and } 10.8$) were smooth, indicating a fine and uniform grain size Φ for these hydrides [57]. The $\text{Pr}_2\text{Co}_7\text{H}_{0.25}$ hydride had the highest extrinsic magnetic properties compared to the other $\text{Pr}_2\text{Co}_7\text{H}_x$ hydrides: $H_c = 6.1$ KOe, $(\text{BH})_{\text{max}} = 5.8$ MGOe, $M_r = 40$ emu/g, and remanence ratio $M_r/M_{\text{max}} = 0.62$. The H_c decreased with x from about 11.5 KOe at $x = 0$ to 0.33 KOe at $x = 10.8$. The M_r values ranged from 42.5 to 40.25 emu/g. The decrease in H_c and $(\text{BH})_{\text{max}}$ as a function of H content could mainly be due to the decrease in magnetocrystalline anisotropy resulting from the H absorption. The main interest lies in the fact that hydrogenation increased T_C by a factor of almost 9.1% for $x = 3.75$ compared with the Pr_2Co_7 compound. The $\text{Pr}_2\text{Co}_7\text{H}_{3.75}$ hydride could be considered as a soft material; it finds its applications in the field of magnetic recording or storage of information.

7. Conclusions

In this work, we studied the microstructure and magnetic properties of the nanocrystalline Pr_2Co_7 , $\text{Pr}_2\text{Co}_{7-x}\text{Fe}_x$, $\text{Pr}_2\text{Co}_7\text{C}_x$, and $\text{Pr}_2\text{Co}_7\text{H}_x$ compounds, which were obtained by high-energy ball milling. The Pr_2Co_7 compound can exist in two polymorphic structures: a hexagonal one of the Ce_2Ni_7 type with a space group of $P6_3/mmc$ (2:7 H structure), which is stable at a relatively low temperature ($T \leq 1023$ K), and a rhombohedral one of the Gd_2Co_7 type with a space group of $R\bar{3}m$ (2:7 R structure), which is stable at a high temperature ($T \geq 1223$ K). The T_C is around 600 K for the 2:7 H structure and 580 K for the 2:7 R one. The study of the magnetocaloric properties of the nanocrystalline Pr_2Co_7 compound showed the presence of a large reversible magnetic entropy change with a second-order magnetic transition. The maximum value (ΔS_M^{max}) was about 3.7 J/(kg.K) under a magnetic

field of 0–16 kOe. The relative cooling power (RCP) was equal to 102.7 J/kg and 8.5 J/kg for the 2:7 R and 2:7 H structures, respectively.

The nanocrystalline $\text{Pr}_2\text{Co}_{7-x}\text{Fe}_x$ compounds annealed at $T_a = 973$ K crystallized into the 2:7 H structure for $x \leq 1$, but for $x \geq 3.5$, the 2:7 phase disappeared completely and decomposes into $\text{Pr}(\text{Co,Fe})_3 + \text{Pr}_2(\text{Co,Fe})_{17}$. The refinement of the EXAFS spectra for ≤ 1 showed that Fe atoms preferably occupied the 12k site in the $\text{Pr}_2\text{Co}_{7-x}\text{Fe}_x$ alloys. This could be related to the fact that the 12k site is significantly more anisotropic in the c direction than the other four Co sites. The study of the magnetic properties of nanocrystalline $\text{Pr}_2\text{Co}_{7-x}\text{Fe}_x$ compounds showed that the T_C was improved by 26% for $x = 0.5$, $H_c = 12$ kOe, $M_r = 43$ emu/g, and $(\text{BH})_{\text{max}} = 9$ MGOe, as well as at 10 K, $H_c = 53$ kOe, $M_r = 43$ emu/g, $(\text{BH})_{\text{max}} = 30$ MGOe. The insertion of C atoms into the Pr_2Co_7 cell led to a marked improvement in T_C of 21.6%. The greatest magnetic properties for the $\text{Pr}_2\text{Co}_7\text{C}_{0.25}$ compound, including an H_c of 10.3 kOe, a remanence ratio M_r/M_s of 0.78, and a $(\text{BH})_{\text{max}}$ of 11.5 MGOe, were found at $T = 293$ K. We investigated the microstructure, hydrogenation, and magnetic properties of nanocrystalline $\text{Pr}_2\text{Co}_7\text{H}_x$ hydrides. Two plateaus were found during the absorption–desorption process in the P–C isotherm. The crystal structure of the Pr_2Co_7 compound transformed from a hexagonal ($P6_3/mmc$) structure to an orthorhombic ($Pbcn$) and monoclinic ($C2/c$) structure during hydrogenation. The absorption of hydrogen by the Pr_2Co_7 compound led to an increase in T_C from 600 K at $x = 0$ to 691 K at $x = 3.75$. The $\text{Pr}_2\text{Co}_7\text{H}_{0.25}$ hydride had the best magnetic properties: $H_c = 6.1$ kOe, $(\text{BH})_{\text{max}} = 5.8$ MGOe, $M_r = 40$ emu/g, and $T_C = 607$ K. We adapted the MFT and RMA methods to investigate the magnetic moments, exchange interactions, and magnetic anisotropy properties. The correlations between microstructure and magnetic properties were discussed. The obtained results could provide a reference for tailoring the magnetic properties of the Pr_2Co_7 , $\text{Pr}_2\text{Co}_{6.5}\text{Fe}_{0.5}$, $\text{Pr}_2\text{Co}_7\text{C}_{25}$, and $\text{Pr}_2\text{Co}_7\text{H}_{0.25}$ compounds for potential permanent nanomagnets, high-density magnetic media, magnetic refrigeration applications, and hydrogen storage.

Author Contributions: Conceptualization, R.F., N.M. and L.B.; resources, R.F., N.M. and L.B.; data analysis and validation, R.F., N.M. and L.B.; original draft preparation, R.F., N.M. and L.B.; review and editing, R.F., N.M. and L.B. All authors have read and agreed to the published version of the manuscript.

Funding: This research received no external funding.

Institutional Review Board Statement: Not applicable.

Informed Consent Statement: Not applicable.

Data Availability Statement: Data sharing not applicable.

Acknowledgments: This research was supported by the CNRS and the “Ministère de l’Enseignement et de la Recherche Scientifique, LR99ES17”. The authors would like to acknowledge the PRF2019-D4P2 and PHC-Utique G211408 projects.

Conflicts of Interest: The authors declare no conflict of interest.

Abbreviations

| | |
|-------|--|
| EDS | Energy-Dispersive X-ray Spectroscopy |
| EXAFS | Extended X-Ray Absorption Fine Structure |
| H_c | Coercive Field |
| HRTEM | High-Resolution Transmission Electron Microscopy |
| M_r | Remanent Magnetization |
| STEM | Scanning Transmission Electron Microscopy |
| T_C | Curie Temperature |
| MFT | Mean Field Theory |
| RMA | Random Magnetic Anisotropy |
| RCP | Relative Cooling Power |

References

1. Burzo, E. Exchange Interactions and Transition Metal Moments in Rare-Earth Compounds. *J. Synch. Investig.* **2018**, *12*, 431–435. [[CrossRef](#)]
2. Zhang, Y. Review of the structural, magnetic and magnetocaloric properties in ternary rare earth RE₂T₂X type intermetallic compounds. *J. Alloys Compd.* **2019**, *787*, 1173–1186. [[CrossRef](#)]
3. Wang, Y.; Guo, D.; Wu, B.; Geng, S.; Zhang, Y. Magnetocaloric effect and refrigeration performance in RE₆₀Co₂₀Ni₂₀ (RE = Ho and Er) amorphous ribbons. *J. Magn. Magn. Mater.* **2020**, *498*, 166179. [[CrossRef](#)]
4. Li, L.; Yan, M. Recent progresses in exploring the rare earth based intermetallic compounds for cryogenic magnetic refrigeration. *J. Alloys Compd.* **2020**, *823*, 153810. [[CrossRef](#)]
5. Yin, L.; Parker, D.S. Effect of atom substitutions on the magnetic properties in Ce₂Fe₁₇: Toward permanent magnet applications. *J. Appl. Phys.* **2021**, *129*, 103902. [[CrossRef](#)]
6. Schafer, L.; Skokov, K.; Liu, J.; Maccari, F.; Braun, T.; Riegg, S.; Radulov, I.; Gassmann, J.; Merschroth, H.; Harbig, J.; et al. Design and Qualification of Pr-Fe-Cu-B Alloys for the Additive Manufacturing of Permanent Magnets. *Adv. Funct. Mater.* **2021**, *31*, 2102148. [[CrossRef](#)]
7. Dirba, I.; Sepehri-Amin, H.; Skokov, K.; Skourski, Y.; Hono, K.; Gutfleisch, O. Magnetic properties and microstructure of Sm₅Fe₁₇-based composite magnets. *Acta Mater.* **2021**, *212*, 116912. [[CrossRef](#)]
8. Jaballah, H.; Bouzidi, W.; Fersi, R.; Mliki, N.; Bessais, L. Structural, magnetic and magnetocaloric properties of (Pr,Sm)₂Fe₁₇ compound at room temperature. *J. Phys. Chem. Solids* **2022**, *532*, 110438. [[CrossRef](#)]
9. Chrobak, A.; Bajorek, A.; Chełkowska, G.; Haneczok, G.; Kwicien, M. Magnetic properties and magnetocaloric effect of the Gd(Ni_{1-x}Fe_x)₃ crystalline compound and powder. *Phys. Status Solidi* **2009**, *206*, 731–737. [[CrossRef](#)]
10. Bajorek, A.; Berger, C.; Pruzik, K.; Zubko, M.K.; Wojtyniak, M.; Chełkowska, G. Novel Ho(Ni_{0.8}Co_{0.2})₃ nanoflakes produced by high energy ball-milling. *Mater. Characterisation* **2017**, *128*, 45–53.
11. Lopadczak, P.; Bajorek, A.; Prusik, K.; Zubko, M.; Chełkowska, G. Magnetic hardening induced in RCo₅ (R = Y, Gd, Sm) by short HEBM. *Acta Phys. Pol. A* **2018**, *55*, 2100904. [[CrossRef](#)]
12. Bajorek, A.; Lopadczak, P.; Prusik, K.; Zubko, M.; Chełkowska, G. The comparison of magnetic properties at room temperature in RCo₅ (R = Y, Sm, Gd) nanoflakes synthesized via time-staged HEBM. *IEEE Trans. Magn.* **2019**, *55*, 2100904. [[CrossRef](#)]
13. Dahal, J.N.; Ali, K.S.S.; Mishra, S.R.; Neupane, D. Effect of Ga and Zr Substitution on the Properties of Dy₂Fe_{17-x}Zr_x and Dy₂Fe₁₆Ga_{1-x}Zr_x (0 ≤ x ≤ 1) Intermetallic Compounds Prepared via Arc Melting Process. *Magnetochemistry* **2020**, *6*, 9. [[CrossRef](#)]
14. Liu, K.; Wang, S.H.; Feng, Y.L.; Zhang, Y.K. Research on Phases and Morphology of Sm₂Fe₁₇ Melt-Spun Ribbon. *Rare Met. Mater. Eng.* **2020**, *49*, 3796–3802.
15. Onoue, M.; Kobayashi, R.; Mitsui, Y.; Umetsu, R.Y.; Uwatoko, Y.; Koyama, K. Magnetic field-induced nitridation of Sm₂Fe₁₇. *J. Alloys Compd.* **2020**, *835*, 155193. [[CrossRef](#)]
16. Veselova, S.; Tereshina, I.; Verbetsky, V.; Neznakhin, D.; Tereshina-Chitrova, E.; Kaminskaya, T.; Karpenkov, A.; Akimova, O.; Gorbunov, D.; Savchenko, A. Structure and magnetic properties of (Sm,Ho)₂Fe₁₇N_x (x = 0; 2.4). *J. Magn. Magn. Mater.* **2020**, *502*, 166549. [[CrossRef](#)]
17. Kovacs, A.; Fischbacher, J.; Gusenbauer, M.; Oezelt, H.; Herper, H.C.; Vekilova, O.Y.; Nieves, P.; Arapan, S.; Schrefl, T. Computational Design of Rare-Earth Reduced Permanent Magnets. *Engineering* **2020**, *6*, 148–153. [[CrossRef](#)]
18. Coey, J.M.D. Perspective and Prospects for Rare Earth Permanent Magnets. *Engineering* **2020**, *6*, 119–131. [[CrossRef](#)]
19. Bajorek, A.; Lopadczak, P.; Prusik, K.; Zubko, M. Correlation between Microstructure and Magnetism in Ball-Milled SmCo₅/α-Fe (5%wt. α-Fe) Nanocomposite Magnets. *Materials* **2021**, *14*, 502. [[CrossRef](#)]
20. Ener, S.; Skokov, K.P.; Palanisamy, D.; Devillers, T.; Fischbacher, J.; Eslava, G.G.; Maccari, F.; Schafer, L.; Diop, L.V.B.; Radulov, I.; et al. Twins—A weak link in the magnetic hardening of ThMn₁₂-type permanent magnets. *Acta Mater.* **2021**, *214*, 116968. [[CrossRef](#)]
21. Opelt, K.; Ahmad, T.; Diehl, O.; Schonfeldt, M.; Brouwer, E.; Vogel, I.; Rossa, J.D.; Gassmann, J.; Ener, S.; Gutfleisch, O. Upscaling the 2-Powder Method for the Manufacturing of Heavy Rare-Earth-Lean Sintered didymium-Based Magnets. *Adv. Eng. Mater.* **2021**, *23*, 2100459. [[CrossRef](#)]
22. Galler, A.; Ener, S.; Maccari, F.; Dirba, I.; Skokov, K.P.; Gutfleisch, O.; Biermann, S.; Pourovskii, L.V. Intrinsically weak magnetic anisotropy of cerium in potential hard-magnetic intermetallics. *NPJ Quantum Mater.* **2021**, *2*, 6. [[CrossRef](#)]
23. Hosokawa, A.; Suzuki, K.; Yamaguchi, W.; Takagi, K. Mechanism of anomalous α-Fe formation from stoichiometric Sm₂Fe₁₇ jet-milled powder during post-pulverization annealing. *Acta Mater.* **2021**, *213*, 116981. [[CrossRef](#)]
24. Shen, B.G.; Liang, B.; Wang, F.W.; Cheng, Z.H.; Gong, H.Y.; Zhang, S.Y.; Zhang, J.X. Magnetic Properties of Sm₂Fe_{17-x}Si_x and Sm₂Fe_{17-x}Si_xC Compounds. *J. Appl. Phys.* **1995**, *77*, 2637. [[CrossRef](#)]
25. Cao, L.; Handstein, A.; Gebel, B.; Schäfer, R.; Müller, K.H. Thermostability of Sm₂(FeGa)₁₇C_y prepared by gas-solid reaction (GSR). *J. Appl. Phys.* **1997**, *81*, 4539. [[CrossRef](#)]
26. van Lier, J.; Kubis, M.; Grünberger, W.; Shultz, L.; Kronmüller, H. High performance Sm_{2+δ}Fe₁₅Ga₂C₂ permanent magnets made by melt spinning and hot pressing. *J. Appl. Phys.* **1998**, *83*, 5549. [[CrossRef](#)]
27. Kubis, M.; Eckert, D.; Gebel, B.; Müller, K.H.; Schultz, L. Intrinsic magnetic properties of Sm₂Fe_{17-x}M_xN_y/C_y (M = Al, Ga or Si). *J. Magn. Magn. Mater.* **2000**, *217*, 14. [[CrossRef](#)]

28. Zheng, C.; Yu, D.; Li, K.; Luo, Y.; Jin, J.; Lu, S.; Li, H.; Mao, Y.; Quan, N. Effect of boron additions on phase formation and magnetic properties of TbCu7-type melt spun SmFe ribbons. *J. Magn. Magn. Mater.* **2016**, *412*, 89–94. [[CrossRef](#)]
29. Luo, Y.; Zhang, K.; Li, K.S.; Yu, D.B.; Ling, J.J.; Men, K.; Dou, Q.Y.; Yan, W.L.; Xie, J.J.; Yang, Y.F. Structure and magnetic behaviors of melt-spun SmFeSiB ribbons and their nitrides. *J. Magn. Magn. Mater.* **2018**, *405*, 214–218. [[CrossRef](#)]
30. Yang, W.; Zha, L.; Lai, Y.; Qiao, G.; Du, H.; Liu, S.; Wang, C.; Han, J.; Yang, Y.; Hou, Y.; et al. Structural and magnetic properties of the $R_{10}Fe_{90-x}Si_x$ alloys with R=Y, Ce, Pr, Nd, Sm, Gd, Tb, Dy, Ho, and Er. *Intermetallics* **2018**, *90*, 8–17. [[CrossRef](#)]
31. Takagi, K.; Jinnō, M.; Ozaki, K. Preparation of TbCu7-type Sm-Fe powders by low-temperature HDDR treatment. *J. Magn. Magn. Mater.* **2018**, *454*, 170–175. [[CrossRef](#)]
32. Wu, G.; Li, H.; Yu, D.; Li, K.; Yan, W.; Yuan, C.; Sun, L.; Luo, Y.; Zhang, K. Effect of niobium substitution on microstructures and thermal stability of TbCu7-type Sm-Fe-N magnets. *J. Rare Earths* **2018**, *36*, 281–286. [[CrossRef](#)]
33. Yan, W.; Quan, N.; Luo, Y.; Yu, D.; Wang, Z.; Wu, G.; Zhang, K. Structure and hard magnetic properties of TbCu7-type $SmFe_{8.95-x}Ga_{0.26}Nb_x$ nitrides. *J. Rare Earths* **2018**, *36*, 165–169. [[CrossRef](#)]
34. Buschow, K.H.J. Magnetic anisotropy of some rare earth-cobalt compounds (R_2Co_7). *J. Less-Common. Met.* **1973**, *33*, 311. [[CrossRef](#)]
35. Givord, D.; Lemaire, R. Magnetic Transition and Anomalous Thermal-Expansion in R_2Fe_{17} Compounds. *IEEE Trans. Magn.* **1974**, *10*, 109–113. [[CrossRef](#)]
36. Buschow, K.H.J. Intermetallic compounds of rare-earth and 3d transition metals. *Rep. Prog. Phys.* **1977**, *40*, 1179. [[CrossRef](#)]
37. Kirchmayr, H.; Poldy, C. Magnetism in rare earth—3d intermetallics. *J. Magn. Magn. Mater.* **1978**, *8*, 1–42. [[CrossRef](#)]
38. Street, R.; Day, R.K.; Dunlop, J.B. Magnetic viscosity in NdFeB and SmCo₅ alloys. *J. Magn. Magn. Mater.* **1987**, *69*, 106. [[CrossRef](#)]
39. Coehoorn, R.; Daalderop, G.H.O. Magnetocrystalline anisotropy in new magnetic materials. *J. Magn. Magn. Mater.* **1992**, *104*, 1081–1085. [[CrossRef](#)]
40. Qi, Q.; Li, Y.P.; Coey, J.M.D. Gas-phase interstitially modified intermetallics $R(Fe_{11}Ti)Z_{1-\delta}$. II. 3d magnetization of the compounds $Y(Fe_{11}Ti)Z_{1-\delta}$ (Z = N, C). *J. Phys. Condens. Matter* **1992**, *4*, 8209. [[CrossRef](#)]
41. Fischer, R.; Kronmüller, H. Static computational micromagnetism of demagnetization processes in nanoscaled permanent magnets. *Phys. Rev. B* **1996**, *54*, 7284. [[CrossRef](#)] [[PubMed](#)]
42. Margarian, A.; Li, H.S.; Dunlop, J.B.; Cadogan, J.M. Structural and magnetic properties of the novel compound Dy₃(Fe,Ti)₂₉. *J. Alloys Compd.* **1996**, *239*, 27. [[CrossRef](#)]
43. Cataldo, L.; Lefevre, A.; Cohen-Adad, M. Elaboration et optimisation d’alliages magnetiques: Sm-Co-Cu-Fe-Zr. Etude par diagrammes de phases. *J. Chim. Phys.* **1997**, *A94*, 1087–1093. [[CrossRef](#)]
44. Hu, J. Volume expansion and Curie temperature enhancement in $R_2Fe_{17}C_x$ compounds. *J. Alloys Compd.* **1999**, *285*, 51. [[CrossRef](#)]
45. Fischer, R.; Kronmüller, H. The role of the exchange interaction in nanocrystalline isotropic Nd₂Fe₁₄B-magnets. *J. Magn. Magn. Mater.* **1999**, *191*, 225. [[CrossRef](#)]
46. Bessais, L.; Dorolti, E.; Djega-Mariadassou, C. Correlation between Sm₂(Fe,Ga)₁₇ and its precursor Sm(Fe,Ga)₉. *J. Appl. Phys.* **2005**, *97*, 013902. [[CrossRef](#)]
47. Bessais, L.; Djega-Mariadassou, C.; Beaunier, P. Effect of nanocrystallization on the structure and the magnetic properties of Nd-Fe-Co-Al-B glassy alloy. *J. App. Phys.* **2006**, *99*, 093906. [[CrossRef](#)]
48. Yartys, V.; Riabov, A.; Denys, R.; Sato, M.; Delaplane, R. Novel intermetallic hydrides. *J. Alloys Compd.* **2006**, *408*, 273. [[CrossRef](#)]
49. Khazzan, S.; Mliki, N.; Bessais, L. Structure and magnetic properties of nanocrystalline Sm_{1-s}(Fe,Mo)_{5+2s}. *J. Appl. Phys.* **2009**, *105*, 103904. [[CrossRef](#)]
50. Bessais, L.; Younsi, K.; Khazzan, S.; Mliki, N. X-ray and intrinsic magnetic properties of nanocrystalline Sm₂(Fe, M)₁₇ (M = Si, Ga, Co, Cr, Zr or Mo). *Intermetallics* **2011**, *19*, 997–1004. [[CrossRef](#)]
51. Khazzan, S.; Mliki, N.; Bessais, L.; Djega-Mariadassou, C. Rare-earth iron-based intermetallic compounds and their carbides: Structure and magnetic behaviors. *J. Magn. Magn. Mater.* **2010**, *322*, 224–229. [[CrossRef](#)]
52. Kowalczyk, A. The intrinsic magnetic properties of R₂Co₇B₃ (R= rare earth) intermetallic compounds. *J. Magn. Magn. Mater.* **1997**, *175*, 279. [[CrossRef](#)]
53. Apostolov, A.; Bozukov, L.; Stanev, N.; Mydlar, T. A change in magnetic properties of R₂Co₇ intermetallic compounds (R = Pr, Sm, Tb and Ho) upon hydrogen absorption. *J. Magn. Magn. Mater.* **1990**, *83*, 286. [[CrossRef](#)]
54. Fersi, R.; Mliki, N.; Bessais, L.; Guetari, R.; Russier, V.; Cabie, M. Effect of annealing on structural and magnetic properties of Pr₂Co₇ compounds. *J. Alloys Compd.* **2012**, *14*, 522. [[CrossRef](#)]
55. Deryagin, A.V. 3d-4f METALLIC COMPOUNDS. Magnetic moment, magnetic anisotropy and spin-reorientation phase transition in (4f-3d)-intermetallic compounds. *J. Phys.* **1979**, *C5*, 165. [[CrossRef](#)]
56. Chrobak, A.; Bajorek, A.; Chełkowska, G. Effect of Tb/Gd substitution on crystal structure and exchange interactions of Gd_{1-x}Tb_xNi₃ intermetallic compounds. *Acta Phys. Pol. A* **2012**, *121*, 1132. [[CrossRef](#)]
57. Fersi, R.; Mliki, N.; Bessais, L. Hydrogenation and the effect of H absorption on structural and magnetic properties of nanocrystalline Pr₂Co₇ alloys. *J. Magn. Magn. Mater.* **2018**, *465*, 220–227. [[CrossRef](#)]
58. Yamkane, Z.; Fersi, R.; Rachid, F.; Moubah, R.; Lassri, H.; Mliki, N.; Bessais, L. Random magnetic anisotropy studies in nanocrystalline Pr₂Co₇H_x (0 < x < 3.75) hydrides. *J. Magn. Magn. Mater.* **2018**, *449*, 461–466.
59. Alouhmy, M.; Moubah, R.; Yamkane, Z.; Abid, M.; Lassri, H. Random magnetic anisotropy approach in amorphous Fe(88.4)Zr(11.6) films: Effects of hydrogen implantation. *J. Non-Cryst. Solids* **2021**, *566*, 120879. [[CrossRef](#)]

60. Dunlap, R.; Small, D.; MacKay, G.; O'Brien, J.W.; Dahn, J.R.; Cheng, Z.H. Materials preparation by ball milling. *J. Can. Phys* **2000**, *78*, 211. [[CrossRef](#)]
61. Fersi, R.; Cabie, M.; Mliki, N.; Bessais, L. Impact of carbon insertion on the microstructure and magnetic properties of nanocrystalline Pr₂Co₇ alloys. *J. Alloys Compd.* **2013**, *576*, 415–423. [[CrossRef](#)]
62. Gal, L.; Charbonnier, V.; Zhang, J.; Goubault, L.; Bernard, P.; Latroche, M. Optimization of the La substitution by Mg in the La₂Ni₇ hydride-forming system for use as negative electrode in Ni-MH battery. *Int. J. Hydrogen Energy* **2015**, *40*, 17017–17020. [[CrossRef](#)]
63. Fersi, R.; Cabie, M.; Mliki, N.; Bessais, L. Effect of annealing temperature on the microstructure of Pr₂Co₇ alloys and its hydrogen absorption-desorption kinetics. *Int. J. Hydrogen Energy* **2019**, *44*, 22011–22021. [[CrossRef](#)]
64. Rosetti, I.; Ramis, G. Quantification of delivered H₂ by a volumetric method to test H₂ storage materials. *Int J Hydrogen Energy* **2013**, *38*, 13309. [[CrossRef](#)]
65. Zhang, J.; Charbonnier, V.; Madern, N.; Monnier, J.; Latroche, M. Improvement of reversible H storage capacity by fine tuning of the composition in the pseudo-binary systems A_{2-x}La_xNi₇ (A = Gd, Sm, Y, Mg). *J. Alloys Compd.* **2021**, *852*, 157008. [[CrossRef](#)]
66. Rietveld, H. Line profiles of neutron powder-diffraction peaks for structure refinement. *Acta Crystallogr.* **1967**, *22*, 151–152. [[CrossRef](#)]
67. Rietveld, H. A profile refinement method for nuclear and magnetic structures. *J. Appl. Crystallogr.* **1969**, *2*, 65–71. [[CrossRef](#)]
68. Michalowicz, A.; Moscovici, J.; Muller-Bouvet, D.; Provost, K. Max: Multiplatform applications for xafs. *J. Phys. Conf. Ser.* **2009**, *190*, 012034.
69. Bez, R.; Fersi, R.; Zehani, K.; Moscovici, J.; Bessais, L.; Mliki, N.; Fonda, E.; Michalowicz, A. Phase stability, EXAFS investigation and correlation between nanostructure and extrinsic magnetic properties of nanocrystalline Pr₂(Co,Fe)₇. *J. Alloys Compd.* **2016**, *666*, 317. [[CrossRef](#)]
70. Ankudinov, A.; Ravel, B.; Rehr, J.; Conradson, S. Real-space multiplescattering calculation and interpretation of x-ray-absorption near-edge structure. *Phys. Rev. B* **1998**, *58*, 7565. [[CrossRef](#)]
71. Fersi, R.; Mliki, N.; Cabié, M.; Bessais, L. Intrinsic and extrinsic magnetic properties of nanocrystalline Pr₂(Co,Fe)₇. *Phys. Status Solidi* **2014**, *211*, 910. [[CrossRef](#)]
72. Charbonnier, V.; Zhang, J.; Monnier, J.; Goubault, L.; Bernard, P.; Magén, C.; Serin, V.; Latroche, M. Structural and Hydrogen Storage Properties of Y₂Ni₇ Deuterides Studied by Neutron Powder Diffraction. *J. Phys. Chem. C* **2015**, *119*, 12218–12225. [[CrossRef](#)]
73. Paul-Boncour, V.; Crivello, J.; Madern, N.; Zhang, J.; Diop, L.; Charbonnier, V.; Monnier, J.; Latroche, M. Correlations between stacked structures and weak itinerant magnetic properties of La_{2-x}Y_xNi₇ compounds. *J. Phys. Condens. Matter* **2020**, *32*, 415804. [[CrossRef](#)] [[PubMed](#)]
74. Provost, K.; Beret, E.C.; Muller, D.; ans A. Michalowicz, E.S.M. Impact of the number of fitted Debye-waller factors on exafs fitting. *J. Phys. Conf. Ser.* **2013**, *430*, 012015. [[CrossRef](#)]
75. Mimault, J.; Fontaine, A.; Lagarde, P.; Raoux, D.; Sadoc, A.; Spanjaard, D. Elastic core effect and clustering tendency by EXAFS in as-quenched Al-Zn alloys. *J. Phys. F Met. Phys.* **1981**, *11*, 1311. [[CrossRef](#)]
76. Iwase, K.; Mashii, S.; Mori, K. Hydrogenation characteristics of Ce₂Ni₇-type La₂Co₇ and its phase transformation during hydrogen absorption-desorption processes. *J. Solid State Chem.* **2021**, *299*, 122201. [[CrossRef](#)]
77. Néel, L. Relation entre la constante d'anisotropie et la loi d'approche à la saturation des ferromagnétiques. *Rep. Prog. Phys.* **1948**, *9*, 148. [[CrossRef](#)]
78. Masrou, R.; Jabar, A.; Khelif, H.; Jemaa, F.B.; Ellouze, M.; Hlil, E.K. Experiment, mean field theory and Monte Carlo simulations of the magnetocaloric effect in La_{0.67}Ba_{0.22}Sr_{0.11}MnO₃ compound. *Solid State Commun.* **2017**, *268*, 64. [[CrossRef](#)]
79. Herzer, G. Grain Size Dependence of Coercivity and Permeability in Nanocrystalline Ferromagnets. *IEEE Trans. Magn.* **2020**, *1397*, 26.
80. Bouzidi, W.; Mliki, N.; Bessais, L. Second-order magnetic transition and low field magnetocaloric effect in nanocrystalline Pr₅Co₁₉ compound. *J. Electron. Mater.* **2018**, *47*, 2776–2781. [[CrossRef](#)]